# NINJ1 mediates plasma membrane rupture by cutting and releasing membrane disks

## Graphical abstract



Cookie cutter model of NINJ1 activation leading to plasma membrane rupture

NINJ1 belt around a membrane disk

NINJ1 oligomers "cut" membrane into pieces

NINJ1 "Ninja" "cutters"

Plasma membrane rupture as a result of NINJ1 activation and oligomerization

NINJ1 "Ninja" "cutters"

## Authors

Liron David, Jazlyn P. Borges, L. Robert Hollingsworth, ..., Evelyn Garlick, Benjamin E. Steinberg, Hao Wu

## Correspondence

wu@crystal.harvard.edu

## In brief

Pyroptosis is a form of signaling-induced cell death characterized by plasma membrane rupture. This study suggests a "cookie cutter"-like mechanism for pyroptotic cell lysis in which oligomerization of the protein NINJ1 punches holes out of the plasma membrane and liberates "cookie"-like disks.

## Highlights

- NINJ1 contains transmembrane helices with kinks and forms a chain-like oligomer

- NINJ1 oligomer structure has a hydrophobic, concave side for membrane interaction

- NINJ1 dissolves liposomes and forms ring-like structures in activated macrophages

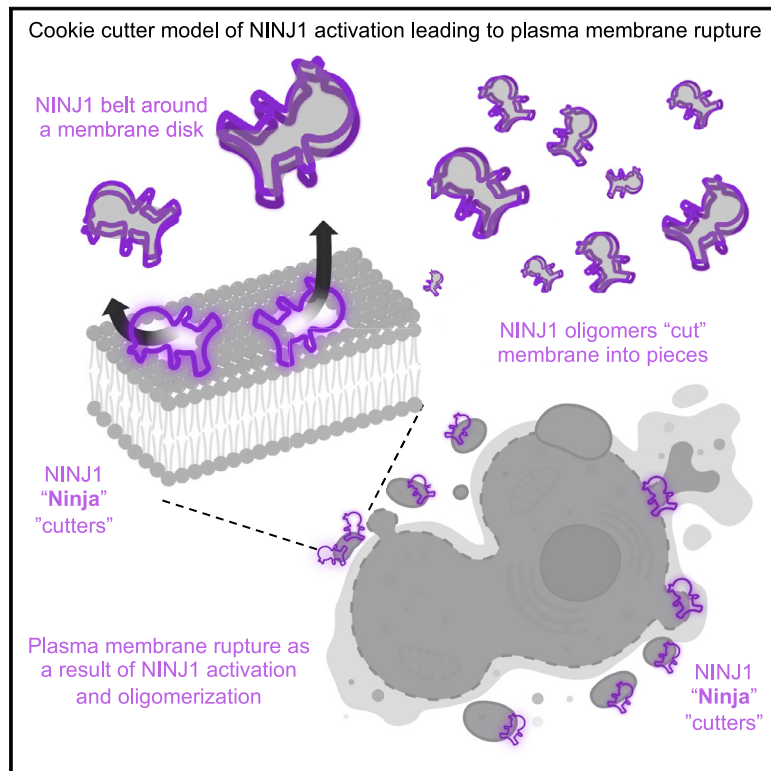- Upon pyroptosis, NINJ1 cuts and sheds membrane disks, acting like a cookie cutter

CellPress

## Article

# NINJ1 mediates plasma membrane rupture by cutting and releasing membrane disks

Liron David,[1,2,9] Jazlyn P. Borges,[3,4] L. Robert Hollingsworth,[1,2,10] Allen Volchuk,[5] Isabelle Jansen,[6] Evelyn Garlick,[6] Benjamin E. Steinberg,[3,4,7,8] and Hao Wu[1,2,11,*]

[1]Department of Biological Chemistry and Molecular Pharmacology, Harvard Medical School, Boston, MA, USA
[2]Program in Cellular and Molecular Medicine, Boston Children's Hospital, Boston, MA, USA
[3]Department of Physiology, Temerty Faculty of Medicine, University of Toronto, Toronto, ON, Canada
[4]Program in Neuroscience and Mental Health, Hospital for Sick Children, Toronto, ON, Canada
[5]Program in Cell Biology, Hospital for Sick Children, Toronto, ON, Canada
[6]Abberior Instruments GmbH, Göttingen, Germany
[7]Department of Anesthesia and Pain Medicine, Hospital for Sick Children, Toronto, ON, Canada
[8]Department of Anesthesiology and Pain Medicine, Temerty Faculty of Medicine, University of Toronto, Toronto, ON, Canada
[9]Present address: Department of Life Sciences, Ben-Gurion University of the Negev, Be'er Sheva, Israel
[10]Present address: Department of Cell Biology, Harvard Medical School, Boston, MA, USA
[11]Lead contact
*Correspondence: wu@crystal.harvard.edu
https://doi.org/10.1016/j.cell.2024.03.008

## SUMMARY

The membrane protein NINJ1 mediates plasma membrane rupture in pyroptosis and other lytic cell death pathways. Here, we report the cryo-EM structure of a NINJ1 oligomer segmented from NINJ1 rings. Each NINJ1 subunit comprises amphipathic ($\alpha$1, $\alpha$2) and transmembrane (TM) helices ($\alpha$3, $\alpha$4) and forms a chain of subunits, mainly by the TM helices and $\alpha$1. $\alpha$3 and $\alpha$4 are kinked, and the Gly residues are important for function. The NINJ1 oligomer possesses a concave hydrophobic side that should face the membrane and a convex hydrophilic side formed by $\alpha$1 and $\alpha$2, presumably upon activation. This structural observation suggests that NINJ1 can form membrane disks, consistent with membrane fragmentation by recombinant NINJ1. Live-cell and super-resolution imaging uncover ring-like structures on the plasma membrane that are released into the culture supernatant. Released NINJ1 encircles a membrane inside, as shown by lipid staining. Therefore, NINJ1-mediated membrane disk formation is different from gasdermin-mediated pore formation, resulting in membrane loss and plasma membrane rupture.

## INTRODUCTION

The Ninjurin (NINJ) family comprises transmembrane (TM) proteins originally discovered as adhesion molecules important for promoting axonal growth upon injury.[1] It is now known that these proteins are widely expressed in both adult and embryonic tissues and play important roles both within and beyond the nervous system.[2] In mammals, there are two NINJ family members, NINJ1 and NINJ2, which share conserved TM regions and ~55% overall sequence homology but have no significant homology to any other known proteins. NINJ1 and NINJ2 exhibit a predicted domain architecture that comprises an N-terminal region, an amphipathic helical region, and two conserved hydrophobic TM helices at the C-terminal region[3] (Figure 1A). The N-terminal region was shown to mediate the cell adhesion and neurite extension function of NINJ1.[2,4] The cell adhesion function of NINJ1 is also important for the progression of inflammation by promoting migration of myeloid cells to inflammatory lesions.[5,6] NINJ1 is a target of p53 and appears to exhibit complex functions in systemic inflammation and tumorigenesis.[7]

Inflammasomes are supramolecular complexes that activate caspase-1 or other inflammatory caspases, which in turn cleave and activate the pore-forming protein gasdermin D (GSDMD) to induce pyroptosis, a lytic form of cell death.[8,9] A recent study showed that GSDMD pore formation is not sufficient to induce the plasma membrane rupture (PMR) critical for lytic cell death and the full release of damage-associated molecular patterns (DAMPs) such as HMGB1 as well as the PMR marker lactate dehydrogenase (LDH).[3] By contrast, NINJ1, but not NINJ2, is required for LDH release downstream of GSDMD activation in pyroptosis or other forms of lytic cell death.[3] This process was suggested to involve NINJ1 oligomerization on the plasma membrane to induce membrane rupture; however, despite the functional demonstration of its importance, the mechanism by which NINJ1 oligomerizes and elicits membrane rupture remained unclear.

During the preparation of this manuscript, Degen et al. published a NINJ1 structure in the form of a double filament stacked at the hydrophobic face.[10] Unlike our curved NINJ1 oligomer, the structure of the NINJ1 oligomer is straight. The
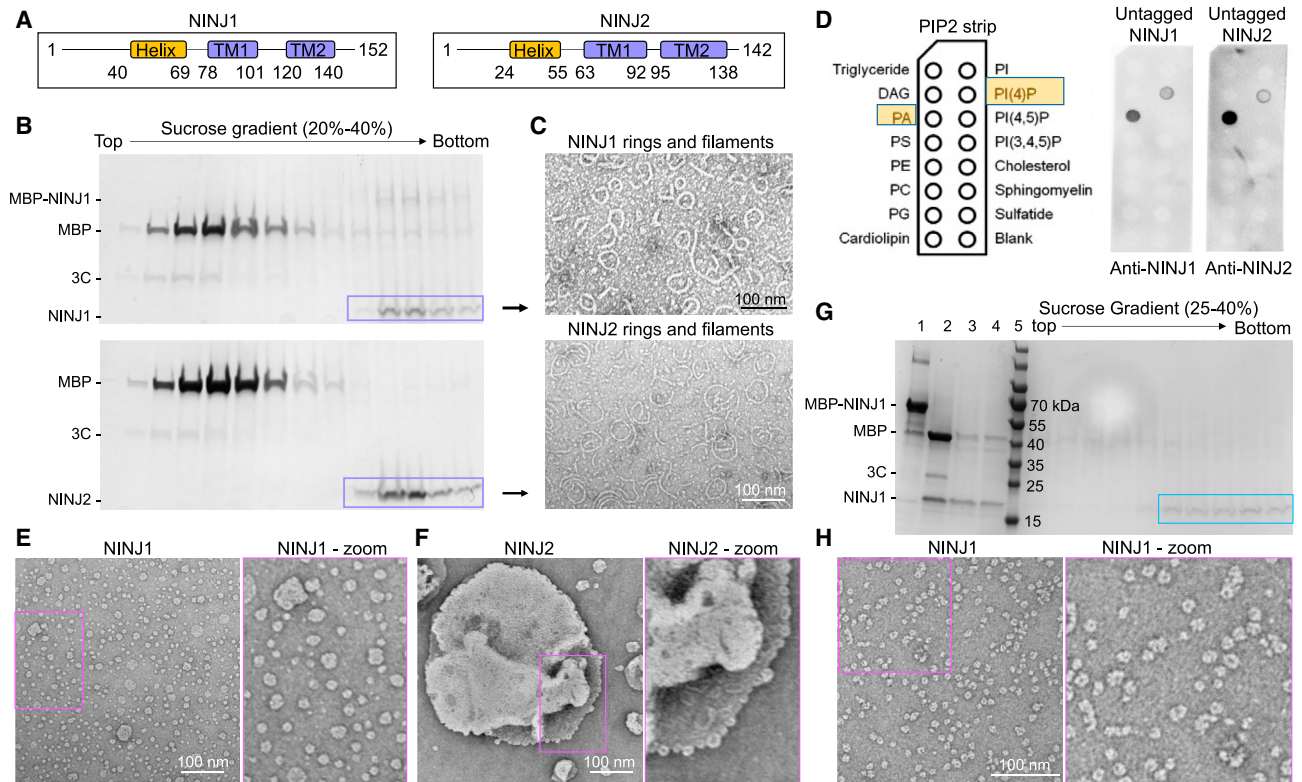
**Figure 1. Formation of rings by NINJ1 and NINJ2 and membrane breakage by NINJ1, not NINJ2**

(A) Domain architectures of human NINJ1 and NINJ2.

(B) Purification of MBP-NINJ1 and MBP-NINJ2 in detergent. SDS-PAGE of NINJ1 and NINJ2 oligomers, purified from the heavy fractions of sucrose gradients after MBP removal.

(C) Negative staining EM of NINJ1 and NINJ2 revealed that they both form rings in detergent.

(D) Lipid strip assays for NINJ1 and NINJ2, showing that they bind negatively charged lipids, specifically PA and PI(4)P.

(E and F) Incorporation of NINJ1 (E) and NINJ2 (F) into liposomes containing PA and PI(4)P, shown by negative staining EM images and their zoom-in views. NINJ1 broke down the liposomes.

(G) Further purification of NINJ1 small rings from liposomes after pelleting using sucrose gradient ultracentrifugation, shown by SDS-PAGE of the fractions (lanes at right). Lanes 1–5: His-MBP-NINJ1, cleaved His-MBP-NINJ1 by 3C, pelleted NINJ1 with lipid, pelleted NINJ1 with lipid solubilized by LMNG, and MW markers.

(H) Negative staining EM of NINJ1 small rings isolated from the sucrose gradient in (G); this same sample was used for cryo-EM studies.

All data are representative of three or more independent experiments.

See also Figure S1.

authors concluded that NINJ1 single filament damages the membrane by capping membrane edges and that NINJ1 pores generate hydrophilic conduits, leading to DAMP release. Here, our structural and imaging data support a different model in which NINJ1, upon activation, forms a hydrophilic side to encircle membrane patches and release them, leading to membrane fragmentation and loss, resulting in complete PMR.

## RESULTS

### NINJ1 and NINJ2 form rings and filaments in detergents

NINJ1 and NINJ2 are small proteins with molecular weights of 16.3 and 15.7 kDa, respectively (Figure 1A). To address the molecular mechanism of NINJ1 function, we overexpressed NINJ1 and NINJ2, N-terminally tagged with a polyhistidine and maltose-binding protein (His-MBP) tag cleavable by the rhino-

virus 3C protease, in *E. coli*. We purified NINJ1 and NINJ2 by amylose resin in the detergent mixture lauryl maltose neopentyl glycol with cholesteryl hemisuccinate (LMNG:CHS = 10:1) and isolated NINJ1 and NINJ2 oligomers after His-MBP removal at the heavy fractions from sucrose gradient ultracentrifugation (Figures 1B and S1A). Surprisingly, NINJ1 and NINJ2 both formed heterogeneous irregular rings and curved filaments, as visualized by negative staining electron microscopy (EM) (Figure 1C). By contrast, the His-MBP tag greatly reduced the ability of NINJ1 to form oligomers (Figure S1B), likely due to a steric inhibition of oligomerization by the large tag. Similarly, we purified NINJ1 tagged at the C terminus with a GFP-FLAG tag expressed in the human cell line Expi293; NINJ1 formed similar irregular rings and curved filaments when isolated by sucrose gradient ultracentrifugation after removal of the GFP-FLAG tag using the tobacco etch virus (TEV) protease (Figures S1C and S1D).
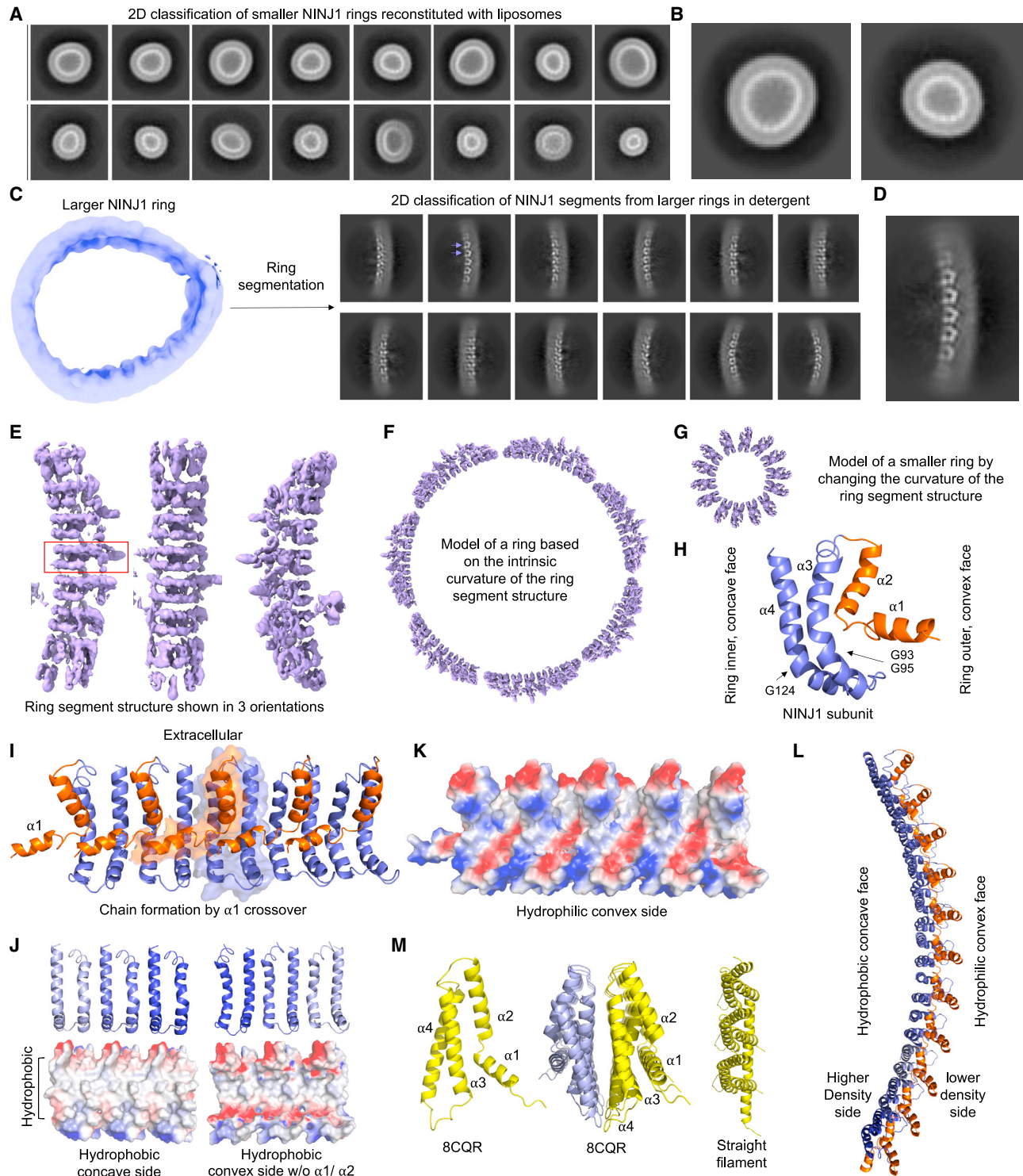
**Figure 2. Cryo-EM studies and structure analysis of NINJ1 rings**

(A) 2D classification of smaller NINJ1 rings reconstituted with liposomes, showing heterogeneous rings.

(B) Magnified images of 2 classes from (A).

(C) Left: irregular large rings in detergents, as represented by a low-resolution 3D reconstruction. These rings were segmented into short segments as single particles. Right: 2D classification of NINJ1 segments, showing clear secondary structure details. A pair of arrows point to TM α-hairpins in two neighboring subunits.

*(legend continued on next page)*

## NINJ1, but not NINJ2, breaks down liposome membranes

Because NINJ1 ruptures membranes,[3] we aimed to reconstitute NINJ1 assemblies using liposomes. For this purpose, we first identified specific lipids that NINJ1 and NINJ2 bind, using lipid strip assays and recombinant, untagged NINJ1 and NINJ2 (Figure 1D). We found that both NINJ1 and NINJ2 interacted with negatively charged lipids: phosphatidic acid (PA), which is the precursor of most phospholipids, and phosphatidylinositol 4-phosphate (PI(4)P), despite having contrasting isoelectric points (PI) of 5.8 (NINJ1) and 9.5 (NINJ2). We then mixed liposomes containing phosphatidylcholine (PC, a major polar lipid), PA, and PI(4)P with His-MBP-NINJ1 and the 3C protease and incubated the mixture at 4°C overnight to allow NINJ1 oligomerization and incorporation into liposomes upon His-MBP tag removal.

Strikingly, negative staining EM analysis revealed that most liposomes were "dissolved" by NINJ1, leaving smaller but heterogeneous structures that likely contain both lipids and NINJ1 in contrast to large liposomes, before mixing with NINJ1 (Figures 1E and S1E). Further magnification suggested that these small structures mimic the smaller irregular rings also observed in detergents (Figures 1C and 1E). By contrast, when we performed the same assay for NINJ2, we detected irregular rings and filaments by negative staining EM, similar to the ones formed in detergents. In this case, however, the NINJ2 rings and filaments sat on liposomes without breaking them like NINJ1 (Figure 1F). Thus, these data suggest the surprising possibility that NINJ1 ruptures membranes by cutting them into small pieces, leading to lytic cell death and a more complete release of DAMPs.

## 2D classes of small NINJ1 rings and structure of a NINJ1 oligomer by cryo-EM

We first pursued cryoelectron microscopy (cryo-EM) structure determination of the small rings from liposome reconstitution. To enhance the sample quality and homogeneity, we solubilized the mixture containing liposomes and NINJ1 with LMNG/CHS, followed by purification over sucrose gradient ultracentrifugation (Figure 1G), which enriched the small irregular NINJ1 rings formed upon mixing with liposomes (Figure 1H). Two-dimensional (2D) classification revealed rings of different sizes and shapes on top or bottom views, as well as certain details that may indicate the different subunits in the assemblies

(Figures 2A, 2B, and S2A). The heterogeneity of the data precluded high-resolution three-dimensional (3D) reconstruction.

To find an alternative route to obtain a NINJ1 structure, we hypothesized that larger and smaller ring structures are assembled by similar mechanisms because they coexist in detergents and because of the similar features of the smaller NINJ1 rings in detergents and from liposomes. Thus, we pursued the cryo-EM structure of the larger rings in detergents. Because of the irregularity of the rings, we picked segments of these rings as single particles that later turned out to contain 6–7 subunits. 2D classification revealed potential secondary structural details from NINJ1 TM hairpins (75–140 aa) (Figures 2C and 2D). 3D reconstruction with C1 symmetry led to a structure of the NINJ1 segment at 4.3 Å resolution (Figures 2E and S2B–S2E). The natural curvature of the ring segment allowed us to generate models illustrating how rings may be formed by repeating these segments (Figure 2F) or how rings of other sizes may be formed by changing the angle at which the neighboring subunits interact (Figure 2G).

Model building using the helical features of the density resulted in a subunit structure that comprised 2 amphipathic helices (37–70 aa, α1 and α2) that are roughly 90° to each other and a pair of TM helices (78–104 for α3, 113–140 for α4) (Figure 2H). The N-terminal segment critical for cell adhesion but not pyroptosis was disordered and not seen in our structure. Strikingly, α3 and α4 are both kinked rather than straight, with glycine (Gly) residues at the exact kink regions: G93 and G95 in α3 and G124 in α4. NINJ1 subunits interact with one another by the placement of the TM helices consecutively and by the crossover of α1 of one subunit to the TM helices of its adjacent subunit, as if extending out a hand (Figure 2I). These interactions could play important roles in NINJ1 oligomerization.

NINJ1 is a constitutive membrane protein with a signal sequence, and its membrane localization is consistent with the hydrophobic nature of α3 and α4 on both the concave and the convex sides of the segment in the absence of α1 and α2 (Figure 2J). The insertion of α1 and α2, which presumably occurs during NINJ1 activation, converts the convex side of the NINJ1 assembly from hydrophobic to hydrophilic (Figure 2K). Thus, the linear NINJ1 oligomers are amphipathic, and as they assemble into rings, the inner concave side is hydrophobic, while the outer convex side is hydrophilic (Figure 2L). This characteristic is likely determined by the natural tendency of the structures, as the curvature of NINJ1 oligomers is conserved in all

---

(D) A magnified 2D class of NINJ1 segments.

(E) Final electron density map of NINJ1 ring segment at 4.3 Å resolution, shown in three views.

(F and G) Modeled NINJ1 rings from the natural curvature of the ring segment (F) and from a more acute curvature to construct smaller rings (G).

(H) Cartoon representation of a NINJ1 monomeric subunit. Amphipathic helices α1 and α2 are in orange, and TM helices α3-α4 are in deep purple. Its relative orientations in a NINJ1 ring are illustrated. α3 and α4 are kinked at Gly residues.

(I) Ribbon representation of 5 NINJ1 subunits in the NINJ1 ring segment. The middle subunit has a transparent surface over the ribbon diagram. The α1 helix extends over to the neighboring subunit to form a chain.

(J) Ribbon representations (top) and electrostatic potentials (bottom) of NINJ1 concave side (left) and convex side (right) for the TM helices alone.

(K) Electrostatic potential of the hydrophilic, convex NINJ1 surface shown in (I).

(L) Model of a longer NINJ1 ring segment viewed from the extracellular side by propagating the ring segment oligomer, showing the clear curvature, the hydrophobic concave face with higher density, and the hydrophilic convex face with lower density. The subunit in (H) has to rotate by ~45° along the vertical axis, followed by a ~90° rotation along the horizontal axis, to arrive at the orientation here.

(M) Stacking in the NINJ1 double filament structure and the resulting straight TM helices and straight filament (PDB: 8CQR).[10]

See also Figures S2 and S3.

2D classes, with the higher density side representing the TM helices at the concave side (Figures 2C, 2D, S3A, and S3B). These data support the idea that when α1 and α2 are inserted into the convex side, a NINJ1 "belt" is formed around a membrane patch and severs it from the bulk membrane, leading to the release of membrane disks.

Our structure of the NINJ1 subunit (PDB: 8UIP) is similar to that by Degen et al. (PDB: 8CQR),[10] with two apparent differences (Figure 2M). First, the 8CQR structure was solved as stacked NINJ1 double filaments, within which each filament is straight and stacks with the opposing filament using the hydrophobic surface. Second, the TM helices in 8CQR are straight rather than kinked, and they provide most of the stacking interactions in a doubling filament.

## NINJ1 forms rings and is released from THP-1 cells during pyroptosis

To further investigate the mechanism of cell lysis by NINJ1 assemblies, we performed cellular imaging studies using the human monocytic cell line, THP-1, differentiated into macrophages by phorbol 12-myristate-13-acetate (PMA). We used CRISPR-Cas9 to generate clonal NINJ1 knockout (KO) cells (clones 37–39) in this background, which we validated by western blot and genomic sequencing (Figures S3C and S3D). We then reconstituted these cells (clone 39) with NINJ1-GFP under a doxycycline (Dox)-inducible promoter. We noted that in addition to cell surface localization, NINJ1-GFP also clustered in intracellular compartments that co-localized with the Golgi marker GM130 but not with the mitochondrial marker MitoTracker (Figures S4A and S4B). The apparent Golgi co-localization was confirmed by immunofluorescence in NINJ1 KO mouse immortalized bone-marrow-derived macrophages (iBMDMs) reconstituted with influenza hemagglutinin (HA)-tagged NINJ1 (Figure S4C) and is consistent with previous observations.[3]

In the absence of Dox induction, nigericin-induced NLRP3 inflammasome activation shown by speck formation of the adaptor protein (ASC) upstream of PMR still occurred robustly but was further enhanced by Dox induction of NINJ1 for 24 h (Figures 3A and S4D). The latter may be consistent with the role of membrane damage and K⁺ efflux in NLRP3 activation.[11–13] Interestingly, the intensity of NINJ1-GFP was reduced upon NLRP3 activation relative to Dox induction without LPS and nigericin treatment when imaged under the same settings (Figure 3B), indicating that NINJ1 was potentially liberated into the culture media. This observation was dependent on NLRP3 activation and was not shown in cells pretreated with the NLRP3 inhibitor MCC950[14] (Figure S4E). NINJ1 did not co-localize with GSDMD (Figure S4F). In addition to the plasma membrane, NINJ1 appeared to localize in membrane extensions from the THP-1 cell surface in LPS-primed cells as well as in NLRP3-activated cells before complete membrane rupture (Figure 3C).

To further capture the live events of NINJ1 during NLRP3 activation, we recorded confocal time-lapse movies of lytic cell death in Dox-induced and LPS-primed THP-1 cells upon nigericin stimulation, from time 0 to 66 min (Figure 3D; Video S1). During this process, the formation and release of NINJ1-positive entities into the culture media were observed throughout. Some of these entities had strong NINJ1-GFP fluorescence at the rim, suggesting that they were likely NINJ1-enclosed membrane disks, although we could not be certain that they were not other types of membrane blebs generated during pyroptosis. Much smaller NINJ1 rings analogous to those observed under negative staining EM are under the diffraction limit of light microscopy and may not be seen. For the cell shown, total catastrophic membrane rupture appeared to have taken place between 58 and 60 min, likely upon reaching a threshold in NINJ1-mediated membrane damage.

## Released NINJ1 rings are membrane disks

Our imaging studies suggested that NINJ1 could become liberated into the cell culture medium during inflammasome activation. To further characterize NINJ1 localization, we induced NINJ1-GFP expression with Dox in THP-1 cells and fractionated the cell pellet and supernatant with a low-speed spin (500 × g, 1 h). We then performed an anti-NINJ1 western blot after running the cell pellet and the supernatant on non-reducing SDS-PAGE (Figure 4A). NINJ1 was only detected in Dox-induced cells, mainly in the cell pellets in untreated or LPS-treated cells as monomers. Strikingly, upon nigericin stimulation, the cell pellet lost most NINJ1, and the supernatant now contained oligomerized NINJ1, supporting NINJ1-GFP shedding to the supernatant after inflammasome activation. We next performed a high-speed spin (136,000 × g, 1 h) of the low-speed spin supernatant, a condition for pelleting cellular membranes, and found that NINJ1-GFP pelleted with the membrane fraction (Figure 4B). We tried to visualize the THP-1 cell supernatant using negative staining EM. The EM images revealed many disk-like entities that may be filled with membranes (Figure 4C), although we could not conclude for sure that these disks were NINJ1-containing structures.

To further visualize the THP-1 supernatant, we stained it with the lipid-interacting BODIPY dye and examined it for the co-localization of NINJ1-GFP and BODIPY (Figure 4D). Many NINJ1-positive structures were visible, ranging in size and shape—some round or oval and others more irregular. Remarkably, almost all NINJ1-positive structures also had BODIPY staining and vice versa, which could suggest that most membrane entities in the supernatant were NINJ1-induced. In addition, the BODIPY stain mostly filled the structures, while the NINJ1-GFP fluorescence was often concentrated at the edge. To confirm this observation, we examined in more detail three representative structures and generated line plots for NINJ1-GFP and for BODIPY (Figures 4E–4G). These plots validated our visual observation that NINJ1-containing entities were often filled with lipid membranes.

## Structure-guided mutational analyses of NINJ1 functions

To validate the NINJ1 oligomer structure and the implicated mechanism of NINJ1 function, we performed a series of structure-guided mutagenesis. These include mutations on Gly residues at the kinks of α3 and α4 TM helices, residues at the hydrophobic face or the hydrophilic face, and a positively charged cluster for potential interaction with PI(4)P (Figures 5A and 5B). For all mutations, we examined oligomerization, liposome rupture, cell death, and plasma membrane localization.
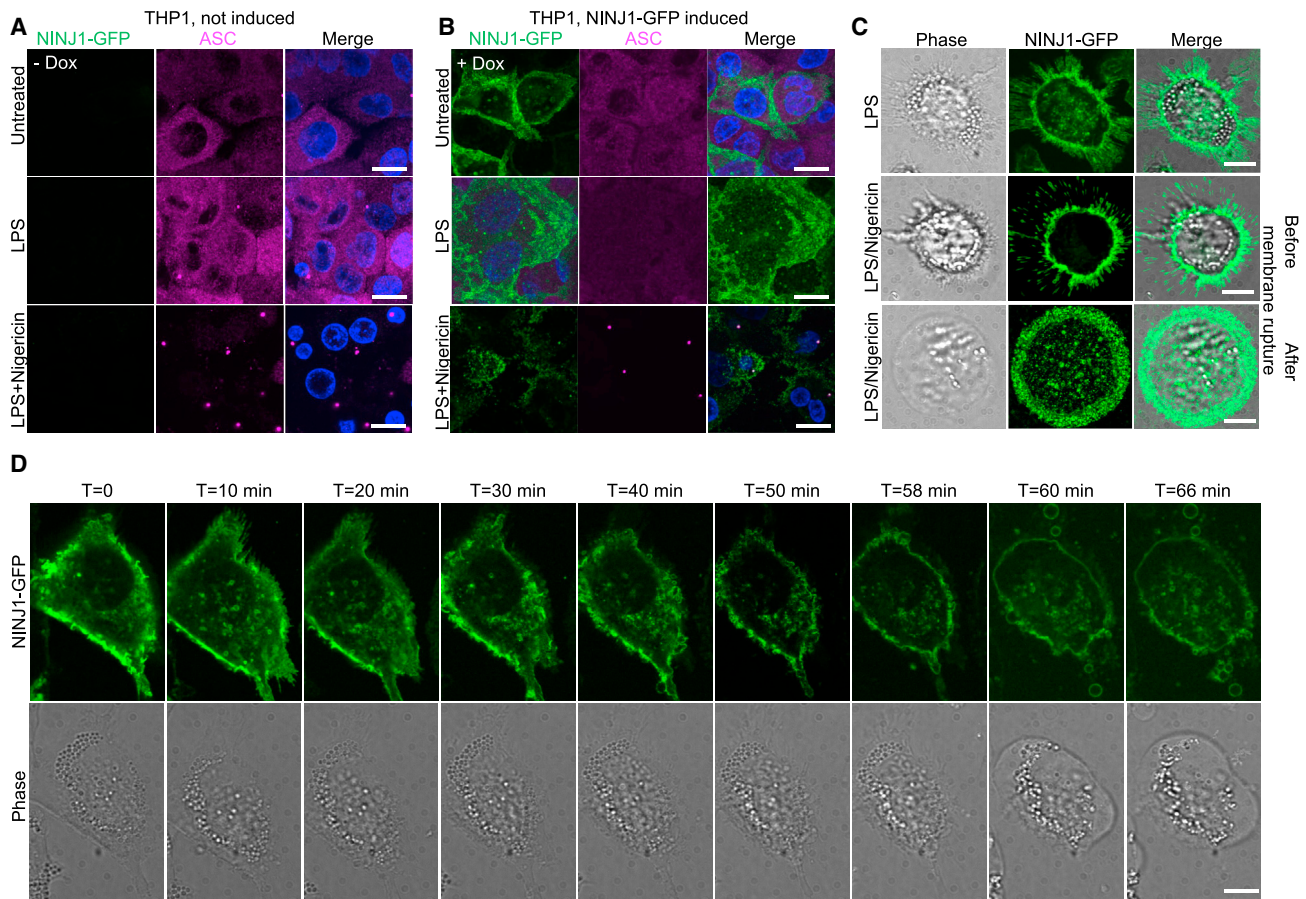
**Figure 3. NINJ1 rings in THP-1 cells**

All scale bars, 10 μM.

(A and B) Fluorescence imaging of NINJ1 KO THP-1 cells reconstituted with NINJ1-GFP for GFP (NINJ1, green), anti-ASC (cyan), and Hoechst (DNA) for vehicle (A) or with doxycycline induction (B). Cells were untreated, primed with LPS (4 h), or primed with LPS (4 h) and treated with nigericin (1 h). Dox-induced cells showed NINJ1 in both untreated and LPS-primed cells. After treatment with nigericin, NINJ1 intensity decreased.

(C) Live cells' fluorescence and phase images of the same THP-1 cells primed with LPS (top) or also treated with nigericin before membrane rupture (middle) and after membrane rupture (bottom).

(D) Time-lapse NINJ1-GFP fluorescence (green) and phase images of the same THP-1 cells imaged for 66 min with 2 min intervals. NINJ1 shedding occurred throughout, and complete cell membrane rupture was captured between 58 and 60 min.

All data are representative of three or more independent experiments.

See also Figures S3 and S4; Video S1.

To address the role of kinks in the TM helices, we mutated G93, G95, and G124 to leucine (Leu) (Figures 5A and 5B), which would disfavor the kinks, and analyzed their phenotypes. Among these Gly mutants, G95L was the most defective, followed by G124L, and G93L showed somewhat suppressed LDH release but did not reach significance in comparison with the wild type (WT) (Figures 5C, 5D, S5A, S5B, and S6A). Interestingly, Degen et al. identified the coevolved F127-G95 pair, and their G95L mutation was also highly defective.[10] None of the Gly mutants had an effect on the cellular localization of NINJ1 at the plasma membrane (Figure S6B), as expected, because we kept the hydrophobicity of these TM helices in the mutants. It may be important to note that the straight TM helices in 8CQR,[10] in contrast to the kinked helices we observed, occurred in the context of two

stacked filaments. Straightening may have occurred in the 8CQR structure to maximize the stacking interface, despite the Gly residues.

Next, we mutated the hydrophilic surface of NINJ1 rings: K44Q, K45Q, and A47L have been analyzed previously,[10] and here, we additionally analyzed K44Q/K45Q double mutant as well as the E49K mutant on the conserved E49 (Figures 5A and 5B). K44Q/K45Q and E49K were highly defective, as shown by oligomerization, liposome rupture, and cell death, while A47L was only borderline defective (Figures 5C, 5D, S5A, S5D, S6A, and S6B). We then mutated the hydrophobic surface of NINJ1 rings (Figures 5C, 5D, S5A, S5C, S6A, and S6B). Degen et al. have mutated part of this membrane-interacting surface at V82 and L121, and it appears that the two sites can tolerate
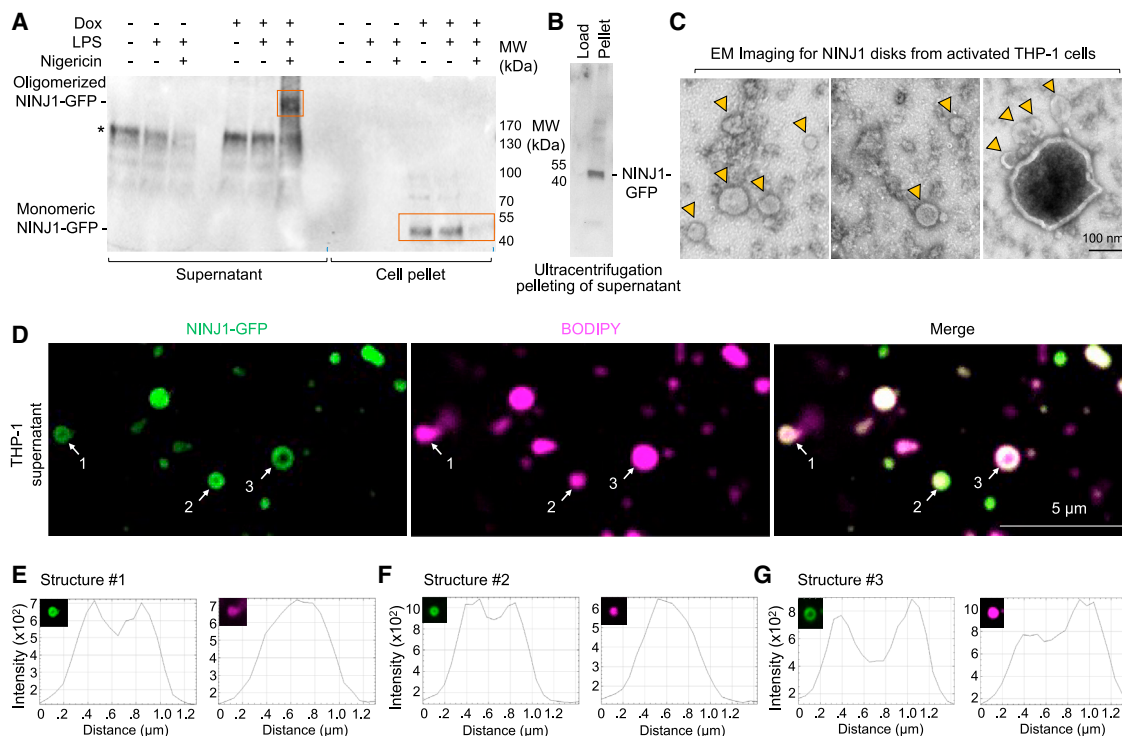
**Figure 4. NINJ1-encircled membrane disks in activated THP-1 supernatant**

(A) Western blots of NINJ1-GFP THP-1 cell pellet and supernatant fractions using anti-NINJ1 on a non-reducing SDS-PAGE. Treatment conditions for each lane are shown. Both NINJ1 oligomers were released to the supernatant after 1 h treatment with nigericin. * indicates non-specific band. Red boxes mark NINJ1 bands.

(B) Ultracentrifugation pelleting of NINJ1-GFP supernatant from activated THP-1 cells.

(C) Negative staining EM images of the supernatant of NINJ1-GFP THP-1 cells after ultracentrifugation, showing membrane-disk-like particles (yellow arrowheads).

(D) Confocal imaging of NINJ1-GFP (green) in THP-1 cell supernatant co-stained with BODIPY lipid stain (magenta). Three NINJ1-containing structures are labeled for (E)–(G). The imaging showed that NINJ1-GFP rings were filled with lipids stained with BODIPY.

(E–G) Line profiles of three ring structures in the field view shown in (D) for both GFP (green) and BODIPY (magenta) channels.

All data are representative of three or more independent experiments.

some—but not necessarily all—mutations that maintain the hydrophobicity.[10] We also mutated I86, L90 (α3), L125, and I128 (α4) in the middle of the TM helices to other hydrophobic residues. L121W was defective, which is consistent with Degen et al., but we did not observe a significant difference in cell killing by V82F. Intriguing, in Degen et al., V82W was not defective, similar to the phenotype of our V82F. Among the new mutations we generated, L90W and L125W were the most defective, followed by I86F, while I128F was only borderline defective. These data suggest that residues at both the hydrophobic and hydrophilic surfaces perform specific roles in NINJ1 oligomerization and pyroptosis.

Furthermore, we mutated a cluster of positively charged residues that could mediate binding to PI(4)P or other acidic lipids: K103E, K111E, and K114E (Figures 5A–D, S5A, S5E, and S6A). While K103E and K111E were highly defective, K114E-mediated cell death was somewhat defective but did not reach a significant difference from the WT. Interestingly, K103E and K111E showed prominent accumulation of NINJ1 intracellularly, with fainter plasma membrane staining, while

other mutants retained plasma membrane localization with much less intracellular staining (Figure S6B). Reduced plasma membrane localization of these mutants could explain the reduced LDH release. However, recombinant K103E, K111E, and K114E still interacted with PI(4)P-containing liposomes (Figure S6C), either due to the higher protein concentrations *in vitro* or due to their lack of defects in PI(4)P binding. Thus, while these data revealed that this cluster of positively charged residues promotes plasma membrane localization, whether the mechanism relates to PI(4)P binding remained unclear.

Finally, we attempted to mutate certain residues in NINJ2 to their corresponding residues in NINJ1, including V86F, Q103F, I110G, and F114I, to identify important determinants for NINJ1's function (Figures 5B and S7A–S7D). All four mutations enhanced NINJ2's activity in membrane rupture and cell killing without affecting their cytoplasmic membrane localization, suggesting that multiple changes may have occurred in evolution, either for NINJ1 to gain or for NINJ2 to lose the membrane rupturing activity.
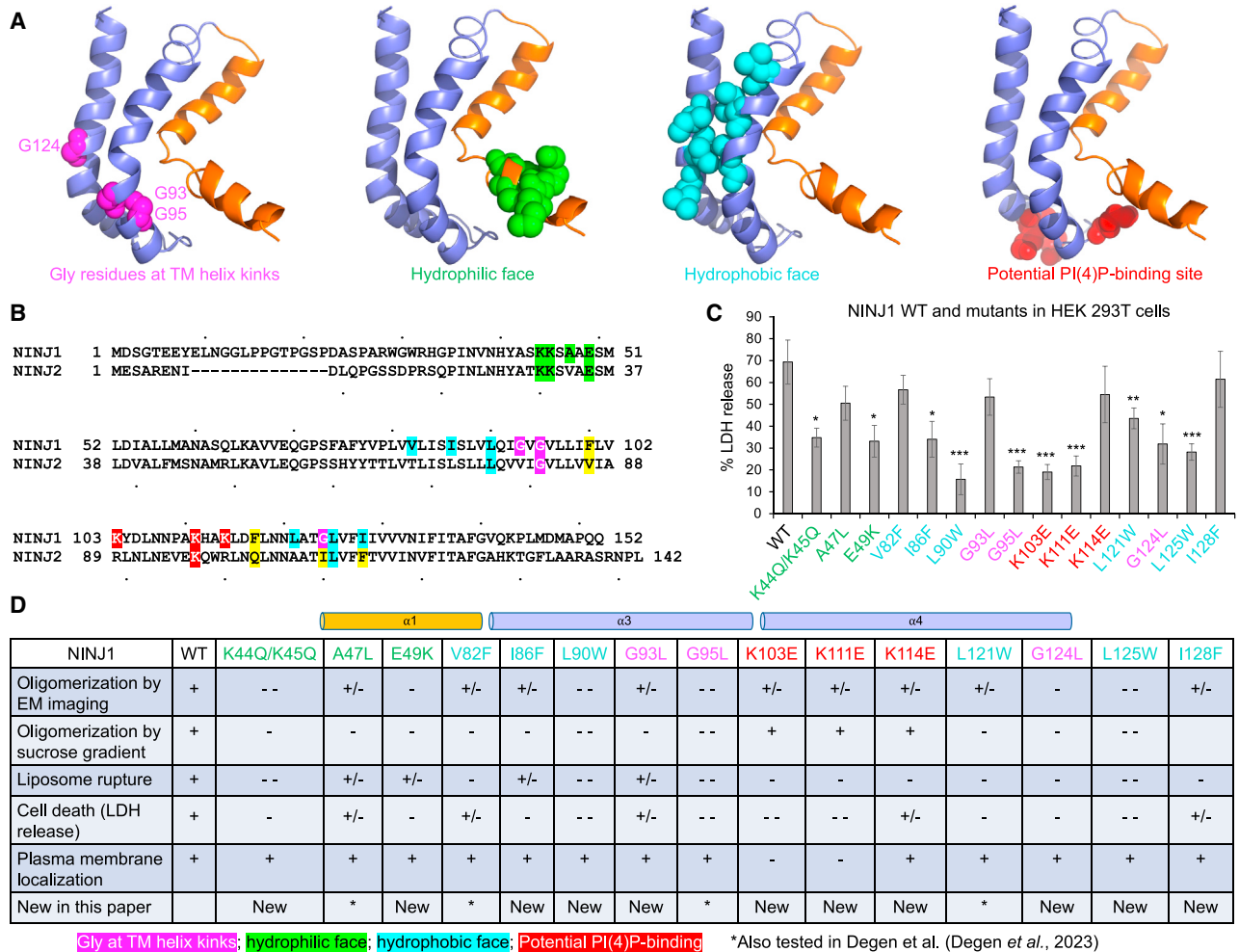
**Figure 5. Mutational analysis of NINJ1**

(A) Ribbon presentation of NINJ1 monomeric subunit highlighting the different types of mutants that were tested. (i) Mutagenesis of Gly residues at the TM kinks, shown in magenta. (ii) Mutagenesis of residues located at the hydrophilic face, shown in green. (iii) Mutagenesis of residues located at the hydrophobic face, shown in cyan. (iv) Mutagenesis of residues in a charged cluster as potential PI(4)P-binding site, shown in red.

(B) Sequence alignment of NINJ1 and NINJ2, with mutated residues highlighted according to colors in (A). Residues in NINJ2 that were mutated to corresponding residues in NINJ1 are highlighted in yellow (Figures S7A–S7D).

(C) Cytotoxicity assay of NINJ1 and mutants in HEK293T cells measured based on % of LDH release, at 24 h post transfection. The data are representative of three or more independent experiments. Statistical significance was assessed by 2-tailed t test. ***,**, and * denote $p < 0.0001$, 0.001, and 0.01, respectively.

(D) A table summarizing the mutational analysis *in vitro* and in cells. The mutants were scored based on the following assays: (i) oligomerization by EM imaging, (ii) oligomerization by sucrose gradient, (iii) liposome rupture, (iv) cell death (LDH release), and (v) plasma membrane localization by confocal imaging.

See also Figures S5–S7.

| NINJ1 | WT | K44Q/K45Q | A47L | E49K | V82F | I86F | L90W | G93L | G95L | K103E | K111E | K114E | L121W | G124L | L125W | I128F |
|---|---|---|---|---|---|---|---|---|---|---|---|---|---|---|---|---|
| Oligomerization by EM imaging | + | -- | +/- | - | +/- | +/- | -- | +/- | -- | +/- | +/- | +/- | +/- | - | -- | +/- |
| Oligomerization by sucrose gradient | + | - | - | - | - | - | -- | - | -- | + | + | + | - | - | -- | |
| Liposome rupture | + | -- | +/- | +/- | - | +/- | -- | +/- | -- | - | - | - | - | - | -- | - |
| Cell death (LDH release) | + | - | +/- | - | +/- | - | -- | +/- | -- | -- | -- | +/- | - | - | -- | +/- |
| Plasma membrane localization | + | + | + | + | + | + | + | + | + | - | - | + | + | + | + | + |
| New in this paper | | New | * | New | * | New | New | New | * | New | New | New | * | New | New | New |

Gly at TM helix kinks; hydrophilic face; hydrophobic face; Potential PI(4)P-binding    *Also tested in Degen et al. (Degen *et al.*, 2023)

## Endogenous NINJ1 clusters into heterogeneous ring-like structures during pyroptosis

In our previous investigations of NINJ1 regulation by the amino acid Gly,[15] we conducted stimulated depletion (STED) super-resolution imaging of endogenous NINJ1 clusters using indirect immunofluorescence in primary mouse BMDMs stimulated to undergo pyroptosis by LPS and nigericin. We achieved an *xy* resolution of 63 ± 8 nm by STED and demonstrated that plasma membrane NINJ1 coalesced into large clusters, following induction of pyroptosis.[15] We did not observe any large clusters in LPS-primed but otherwise inactive cells, where NINJ1 was present in the plasma membrane as small punctate structures.

While we were able to visualize the noted large structures by STED, they represented the minority of NINJ1 clusters. Therefore, we next turned our attention to the major, but smaller, NINJ1 clusters that could not be resolved by STED, using minimal photon fluxes (MINFLUX) nanoscopy.[16,17] By this approach, we were able to obtain a localization precision of 2.8–4.2 nm and 3.6–7.1 nm for 2D- and 3D-MINFLUX, respectively. Representative 2D-MINFLUX images of LPS-primed BMDMs without and with pyroptosis induction are shown, as compared with standard laser scanning confocal microscopy (Figure 6A). The 3D-MINFLUX projection and movie for cells primed with LPS (Figure 6B; Video S2) or treated with LPS
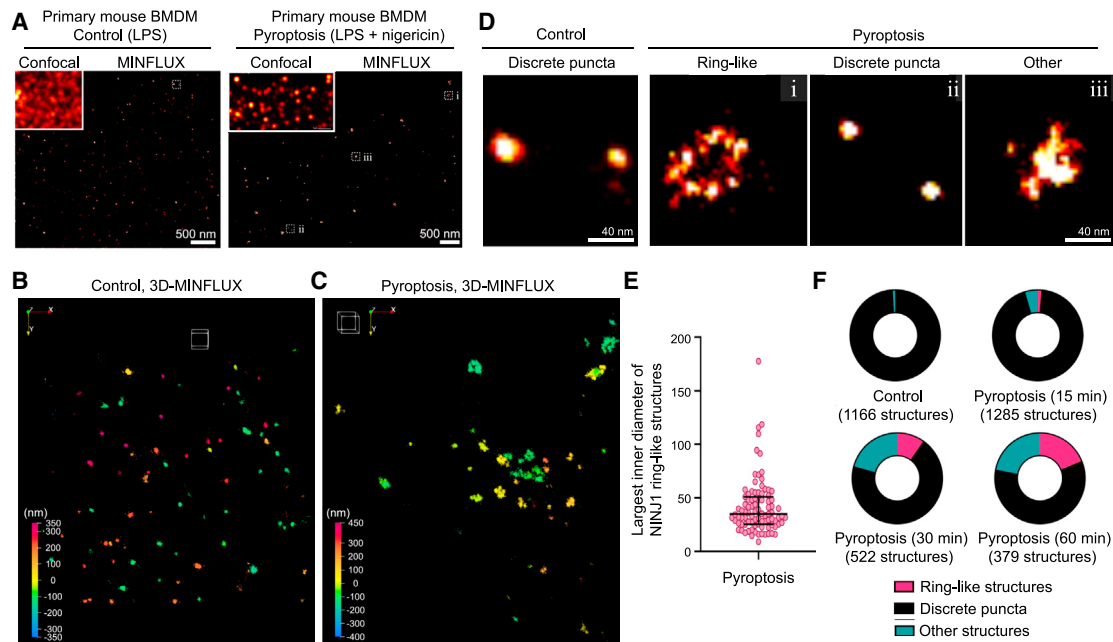
**Figure 6. MINFLUX microscopy demonstrates that NINJ1 forms a heterogeneous population of ring-like structures during pyroptosis**
LPS-primed primary mouse bone-marrow-derived macrophages were stimulated to undergo pyroptosis with nigericin (20 μM, 15–60 min) or left untreated. Cells were fixed in 4% paraformaldehyde and 0.1% glutaraldehyde, followed by immunolabelling with anti-NINJ1 antibody (rabbit monoclonal clone 25, Genentech, Inc) and Alexa Fluor 647-conjugated whole IgG secondary antibody. Samples were then imaged by MINFLUX.
(A) 2D-MINFLUX images (confocal inset) of LPS-primed macrophages without (control, left) or with pyroptosis stimulation (LPS + nigericin, right). Small dashed white boxes indicate images shown in (B). Scale bars, 500 nm.
(B and C) 3D-MINFLUX camera-perspective renderings of heterogenous NINJ1 structures in LPS-primed cells (B) or cells stimulated to undergo pyroptosis (C). The white cube in each has an edge length of 100 nm. The rainbow-colored scale indicates the distance in the Z-plane, which ranges from −350 to +350 nm (B) or −400 to +450 nm (C).
(D) Representative structures of each classification category: ring-like (i), discrete puncta (ii), or other (iii). Scale bars, 40 nm.
(E) Largest measured inner diameter of the identified ring-like structures in the 2D plane ranged from 6 to 178 nm, shown with a median of 32.0 nm (interquartile range, 24.0–48.0 nm).
(F) Pie charts for NINJ1 structures counted and classified as ring-like (i), discrete puncta (ii), or other (iii) for LPS-primed control macrophages and pyroptotic macrophages at different time points.
Data are representative of three independent experiments, except for the pyroptosis (15 min) data in (F), which are representative of two independent experiments.
See also Figure S7; Videos S2 and S3.

plus nigericin (Figure 6C; Video S3) are shown. By MINFLUX, we detected multiple NINJ1 clusters formed in cells stimulated to undergo pyroptosis, which we classified as ring-like (with a central area of zero localizations), punctate (round and without a central area of zero localizations), or other (Figure 6D). Quantification for the largest inner diameters of ring-like structures ranged from 9 to 178 nm, with a median of 34.9 nm (Figure 6E), which overlap in size with the smaller NINJ1 structures released from THP-1 cells (Figure 4D). That the released NINJ1 structures could be larger than those still on the cell surface may suggest that the latter represent precursors of NINJ1 oligomers that were yet to completely sever the membrane. In support of this notion, the appearance of ring-like structures progressed over time (Figure 6F), and the primary BMDM supernatant also contained NINJ1 oligomers, shown by blue-native PAGE upon induction of pyroptosis (Figure S7E). Of note, we did not observe obvious long filament-like structures in cells stimulated to undergo pyroptosis for 30 or 60 min, which corre-

sponds to a time at which point we detected cell rupture. We cannot, however, exclude that some of the punctate or ambiguous structures are filaments. We also performed similar 2D-MINFLUX experiments on secondary necrosis after apoptosis induced by ABT-199, a BCL-2 inhibitor,[18] and observed similar ring-like structures (Figures S7F–S7I).

## DISCUSSION

In this study, we used a combination of structural biology and cellular imaging to investigate the mechanism by which NINJ1 causes membrane lysis. First, we discovered that recombinant NINJ1 alone is sufficient to dissolve liposomes into heterogeneous, ring-like NINJ1-containing assemblies. By contrast, NINJ2 also formed ring-like structures when mixed with liposomes, and they failed to dissolve the liposomes. Second, we determined the cryo-EM structure of a NINJ1 assembly from segments of larger, irregular rings, whose subunit
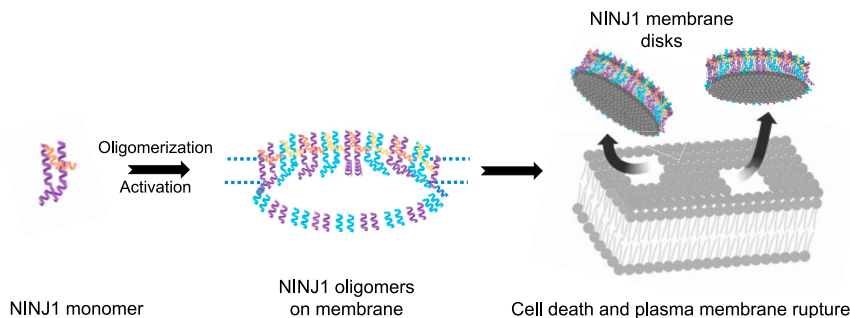
NINJ1 membrane
disks

NINJ1 monomer

Oligomerization
Activation

NINJ1 oligomers
on membrane

Cell death and plasma membrane rupture

structure has the same fold as the published structure.[10] Unlike the published structure, however, which was determined from double filaments bundled together by the hydrophobic side of the filament, our structure from ring segments displays kinked TM helices and an overall curvature of the assembly toward the hydrophobic side. This curvature is observed in all 2D classes and dictates that the inner face of a ring is hydrophobic, making it suitable for membrane binding. Third, mutational analyses confirmed the importance of Gly residues localized at the TM kinks and revealed a cluster of positively charged residues near the inner leaflet of the plasma membrane for NINJ1's proper cell surface localization. Fourth, live-cell imaging of NINJ1 KO human THP-1 cells reconstituted with NINJ1-GFP revealed the release of NINJ1 rings during NLRP3 inflammasome activation into the culture media, and western blot analysis showed the abundance of NINJ1 oligomers in the culture supernatant, but not in cell pellets. Fifth, membrane staining of THP-1 supernatant revealed that NINJ-1 rings are filled with lipids. Finally, super-resolution imaging of endogenous NINJ1 in mouse primary BMDMs identified ring-like structures of various sizes that are consistent with the irregular rings we observed *in vitro*. Importantly, the "chain link" connection between subunits formed by successive crossover of the α1 helix to the adjacent subunit may provide a certain flexibility to accommodate different sizes and shapes.

The collective data we present here illustrates the mechanism by which NINJ1 may cause membrane lysis that is completely different from membrane damage and cargo release by GSDMD pores.[19] This mechanism involves cutting membrane patches within NINJ1 rings and the extraction of the membrane away from the cell surface, a process quite analogous to how certain copolymers such as styrene maleic acid (SMA) can extract membrane proteins into nanodiscs directly from cell membranes by forming a belt around the native lipid bilayer.[20] We propose that the α3 and α4 TM helices already localize NINJ1 to cell membranes in resting state, and a pyroptotic trigger then activates NINJ1, which likely allows the insertion of the α1 and α2 helices, including the crossover to generate stabilized NINJ1 rings with a hydrophilic outer face. By acting like cookie cutters, NINJ1 rings will litter cell membranes with holes, leading to membrane damage and loss; at a threshold point, cells will no longer have enough material or capacity to repair the holes in the membrane, leading to PMR. An amphipathic filament model or pore model with a hydrophilic

conduit[10] may not intuitively explain the lytic function of NINJ1, especially the release of NINJ1 oligomers into the culture media. Even a pore model where NINJ1 pores are larger than those formed by GSDMD would limit the size of its cargos, which may limit DAMP release upon lytic cell death. Thus, our data favor a cookie cutter model, instead of a filament or pore model, for NINJ1-mediated membrane lysis.

### Limitations of the study

Although our study here illustrates a plausible mechanism for NINJ1-mediated membrane rupture, from which we proposed a stepwise process for this function, we do not yet know the details of these steps. In particular, our study does not address how NINJ1 is activated upon induction of lytic cell death. One possibility is ionic influx, such as $Ca^{2+}$ upon GSDMD pore formation. Nonetheless, how does one reconcile live-cell cytokine release through GSDMD pores under certain conditions,[19,21] presumably with $Ca^{2+}$ influx but without NINJ1 activation? Another possibility stems from the unresolved characteristic of large membrane bubbles in NINJ1-deficient cells upon inflammasome activation, which could suggest the involvement of membrane tension. Although myriads of alternative possibilities exist, including the loss of plasma membrane asymmetry during pyroptosis, they remain outside the scope of the presented studies. Finally, we are intrigued by the observation that NINJ2 oligomerizes, yet does not break membranes. More studies are required to elucidate the determinant of this observation and address other important questions related to the small but powerful NINJ1 and NINJ2 proteins.

### STAR★METHODS

Detailed methods are provided in the online version of this paper and include the following:

- KEY RESOURCES TABLE
- RESOURCE AVAILABILITY
  - Lead contact
  - Materials availability
  - Data and code availability
- EXPERIMENTAL MODEL AND SUBJECT DETAILS
  - Cell lines
  - Animals and cells
- METHOD DETAILS
  - Constructs and cloning
  - Protein expression and purification
  - *In vitro* lipid blot assay
  - *In vitro* liposome assay

- ○ Mutagenesis analysis *in vitro* and in cells
- ○ Negative-staining electron microscopy
- ○ Cryo-EM data collection
- ○ Cryo-EM data processing
- ○ Model building and structure representation
- ○ Generation of the HA-NINJ1 cells
- ○ Generation of NINJ1 KO and NINJ1-GFP cell lines
- ○ Pyroptosis and secondary necrosis induction
- ○ Immunoblotting of whole cell lysates
- ○ Blue-native PAGE of NINJ1
- ○ Immunofluorescence (IF)
- ○ Live cell imaging
- ○ Lipid labeling of whole cell lysates
- ○ LDH assay
- ○ Minimal photon fluxes (MINFLUX) nanoscopy
- ○ Mouse NINJ1 co-localization and imaging
- ● QUANTIFICATION AND STATISTICAL ANALYSIS

## SUPPLEMENTAL INFORMATION

Supplemental information can be found online at https://doi.org/10.1016/j.cell.2024.03.008.

## AUTHOR CONTRIBUTIONS

L.D. and H.W. designed and conceptualized the study. L.D. performed cloning, protein purifications, liposome assay, mutagenesis analysis, negative staining EM, cryo-EM sample preparation, screening, data collection, data processing, model building, and refinement. L.D. and L.R.H. generated and validated NINJ1 knockout cell lines. L.R.H. cloned the Dox-inducible NINJ1-GFP construct, and L.D. generated the NINJ1-GFP Dox-inducible cell line. L.D. performed immunoblotting, immunofluorescence microscopy, live-cell imaging, image analysis, and quantifications of microscopy data. J.P.B. performed primary mouse BMDM experiments, LDH assay validation for MINFLUX sample preparation, MINFLUX data analysis, and figure preparation and contributed to manuscript writing, review, and editing. J.P.B. and A.V. prepared primary mouse BMDM cultures, validation, and data curation. I.J. and E.G. performed MINFLUX measurements, methodology, data curation, and MINFLUX image preparation. B.E.S. contributed to conceptualization, data curation, visualization, formal analysis of MINFLUX data, supervision, and funding acquisition and contributed to manuscript writing, review, and editing. L.D. and H.W. wrote the manuscript with input from all authors.

## REFERENCES

1. Araki, T., and Milbrandt, J. (1996). Ninjurin, a novel adhesion molecule, is induced by nerve injury and promotes axonal growth. Neuron *17*, 353–361. https://doi.org/10.1016/s0896-6273(00)80166-x.

2. Araki, T., Zimonjic, D.B., Popescu, N.C., and Milbrandt, J. (1997). Mechanism of homophilic binding mediated by ninjurin, a novel widely expressed adhesion molecule. J. Biol. Chem. *272*, 21373–21380. https://doi.org/10.1074/jbc.272.34.21373.

3. Kayagaki, N., Kornfeld, O.S., Lee, B.L., Stowe, I.B., O'Rourke, K., Li, Q., Sandoval, W., Yan, D., Kang, J., Xu, M., et al. (2021). NINJ1 mediates plasma membrane rupture during lytic cell death. Nature *591*, 131–136. https://doi.org/10.1038/s41586-021-03218-7.

4. Kim, S.W., Lee, H.K., Seol, S.I., Davaanyam, D., Lee, H., and Lee, J.K. (2020). Ninjurin 1 dodecamer peptide containing the N-terminal adhesion motif (N-NAM) exerts proangiogenic effects in HUVECs and in the postischemic brain. Sci. Rep. *10*, 16656. https://doi.org/10.1038/s41598-020-73340-5.

5. Ifergan, I., Kebir, H., Terouz, S., Alvarez, J.I., Lécuyer, M.A., Gendron, S., Bourbonnière, L., Dunay, I.R., Bouthillier, A., Moumdjian, R., et al. (2011). Role of Ninjurin-1 in the migration of myeloid cells to central nervous system inflammatory lesions. Ann. Neurol. *70*, 751–763. https://doi.org/10.1002/ana.22519.

6. Toma, L., Sanda, G.M., Raileanu, M., Stancu, C.S., Niculescu, L.S., and Sima, A.V. (2020). Ninjurin-1 upregulated by TNFalpha receptor 1 stimulates monocyte adhesion to human TNFalpha-activated endothelial cells; benefic effects of amlodipine. Life Sci. *249*, 117518. https://doi.org/10.1016/j.lfs.2020.117518.

7. Yang, H.J., Zhang, J., Yan, W., Cho, S.J., Lucchesi, C., Chen, M., Huang, E.C., Scoumanne, A., Zhang, W., and Chen, X. (2017). Ninjurin 1 has two opposing functions in tumorigenesis in a p53-dependent manner. Proc. Natl. Acad. Sci. USA *114*, 11500–11505. https://doi.org/10.1073/pnas.1711814114.

8. Chou, W.C., Jha, S., Linhoff, M.W., and Ting, J.P. (2023). The NLR gene family: from discovery to present day. Nat. Rev. Immunol. *23*, 635–654. https://doi.org/10.1038/s41577-023-00849-x.

9. Liu, X., Xia, S., Zhang, Z., Wu, H., and Lieberman, J. (2021). Channelling inflammation: gasdermins in physiology and disease. Nat. Rev. Drug Discov. *20*, 384–405. https://doi.org/10.1038/s41573-021-00154-z.

10. Degen, M., Santos, J.C., Pluhackova, K., Cebrero, G., Ramos, S., Jankevicius, G., Hartenian, E., Guillerm, U., Mari, S.A., Kohl, B., et al. (2023). Structural basis of NINJ1-mediated plasma membrane rupture in cell death. Nature *618*, 1065–1071. https://doi.org/10.1038/s41586-023-05991-z.

11. Rühl, S., and Broz, P. (2015). Caspase-11 activates a canonical NLRP3 inflammasome by promoting K(+) efflux. Eur. J. Immunol. *45*, 2927–2936. https://doi.org/10.1002/eji.201545772.

12. Schmid-Burgk, J.L., Gaidt, M.M., Schmidt, T., Ebert, T.S., Bartok, E., and Hornung, V. (2015). Caspase-4 mediates non-canonical activation of the NLRP3 inflammasome in human myeloid cells. Eur. J. Immunol. *45*, 2911–2917. https://doi.org/10.1002/eji.201545523.

13. Yang, D., He, Y., Muñoz-Planillo, R., Liu, Q., and Núñez, G. (2015). Caspase-11 Requires the Pannexin-1 Channel and the Purinergic P2X7 Pore

to Mediate Pyroptosis and Endotoxic Shock. Immunity *43*, 923–932. https://doi.org/10.1016/j.immuni.2015.10.009.

14. Coll, R.C., Robertson, A.A., Chae, J.J., Higgins, S.C., Muñoz-Planillo, R., Inserra, M.C., Vetter, I., Dungan, L.S., Monks, B.G., Stutz, A., et al. (2015). A small-molecule inhibitor of the NLRP3 inflammasome for the treatment of inflammatory diseases. Nat. Med. *21*, 248–255. https://doi.org/10.1038/nm.3806.

15. Borges, J.P., Sætra, R.S.R., Volchuk, A., Bugge, M., Devant, P., Sporsheim, B., Kilburn, B.R., Evavold, C.L., Kagan, J.C., Goldenberg, N.M., et al. (2022). Glycine inhibits NINJ1 membrane clustering to suppress plasma membrane rupture in cell death. eLife *11*, e78609. https://doi.org/10.7554/eLife.78609.

16. Schmidt, R., Weihs, T., Wurm, C.A., Jansen, I., Rehman, J., Sahl, S.J., and Hell, S.W. (2021). MINFLUX nanometer-scale 3D imaging and microsecond-range tracking on a common fluorescence microscope. Nat. Commun. *12*, 1478. https://doi.org/10.1038/s41467-021-21652-z.

17. Tan, Y.H., Liu, M., Nolting, B., Go, J.G., Gervay-Hague, J., and Liu, G.Y. (2008). A nanoengineering approach for investigation and regulation of protein immobilization. ACS Nano *2*, 2374–2384. https://doi.org/10.1021/nn800508f.

18. Souers, A.J., Leverson, J.D., Boghaert, E.R., Ackler, S.L., Catron, N.D., Chen, J., Dayton, B.D., Ding, H., Enschede, S.H., Fairbrother, W.J., et al. (2013). ABT-199, a potent and selective BCL-2 inhibitor, achieves antitumor activity while sparing platelets. Nat. Med. *19*, 202–208. https://doi.org/10.1038/nm.3048.

19. Xia, S., Zhang, Z., Magupalli, V.G., Pablo, J.L., Dong, Y., Vora, S.M., Wang, L., Fu, T.-M., Jacobson, M.P., Greka, A., et al. (2021). Gasdermin D pore structure reveals preferential release of mature interleukin-1. Nature *593*, 607–611. https://doi.org/10.1038/s41586-021-03478-3.

20. Chen, A., Majdinasab, E.J., Fiori, M.C., Liang, H., and Altenberg, G.A. (2020). Polymer-Encased Nanodiscs and Polymer Nanodiscs: New Platforms for Membrane Protein Research and Applications. Front. Bioeng. Biotechnol. *8*, 598450. https://doi.org/10.3389/fbioe.2020.598450.

21. Evavold, C.L., Ruan, J., Tan, Y., Xia, S., Wu, H., and Kagan, J.C. (2018). The Pore-Forming Protein Gasdermin D Regulates Interleukin-1 Secretion from Living Macrophages. Immunity *48*, 35–44.e6. https://doi.org/10.1016/j.immuni.2017.11.013.

22. Morin, A., Eisenbraun, B., Key, J., Sanschagrin, P.C., Timony, M.A., Ottaviano, M., and Sliz, P. (2013). Collaboration gets the most out of software. eLife *2*, e01456. https://doi.org/10.7554/eLife.01456.

23. Punjani, A., Rubinstein, J.L., Fleet, D.J., and Brubaker, M.A. (2017). cryoSPARC: algorithms for rapid unsupervised cryo-EM structure determination. Nat. Methods *14*, 290–296. https://doi.org/10.1038/nmeth.4169.

24. Goddard, T.D., Huang, C.C., Meng, E.C., Pettersen, E.F., Couch, G.S., Morris, J.H., and Ferrin, T.E. (2018). UCSF ChimeraX: Meeting modern challenges in visualization and analysis. Protein Sci. *27*, 14–25. https://doi.org/10.1002/pro.3235.

25. Delano, W.L. (2002). The PyMol Molecular Graphics System. http://pymol.org.

26. Adams, P.D., Afonine, P.V., Bunkóczi, G., Chen, V.B., Davis, I.W., Echols, N., Headd, J.J., Hung, L.W., Kapral, G.J., Grosse-Kunstleve, R.W., et al. (2010). PHENIX: a comprehensive Python-based system for macromolecular structure solution. Acta Crystallogr. D Biol. Crystallogr. *66*, 213–221. https://doi.org/10.1107/S0907444909052925.

27. Mastronarde, D.N. (2005). Automated electron microscope tomography using robust prediction of specimen movements. J. Struct. Biol. *152*, 36–51. https://doi.org/10.1016/j.jsb.2005.07.007.

28. Zheng, S.Q., Palovcak, E., Armache, J.P., Verba, K.A., Cheng, Y., and Agard, D.A. (2017). MotionCor2: anisotropic correction of beam-induced motion for improved cryo-electron microscopy. Nat. Methods *14*, 331–332. https://doi.org/10.1038/nmeth.4193.

29. Rohou, A., and Grigorieff, N. (2015). CTFFIND4: Fast and accurate defocus estimation from electron micrographs. J. Struct. Biol. *192*, 216–221. https://doi.org/10.1016/j.jsb.2015.08.008.

30. Sanchez-Garcia, R., Gomez-Blanco, J., Cuervo, A., Carazo, J.M., Sorzano, C.O.S., and Vargas, J. (2021). DeepEMhancer: a deep learning solution for cryo-EM volume post-processing. Commun. Biol. *4*, 874. https://doi.org/10.1038/s42003-021-02399-1.

31. Pettersen, E.F., Goddard, T.D., Huang, C.C., Couch, G.S., Greenblatt, D.M., Meng, E.C., and Ferrin, T.E. (2004). UCSF Chimera–a visualization system for exploratory research and analysis. J. Comput. Chem. *25*, 1605–1612. https://doi.org/10.1002/jcc.20084.

32. Emsley, P., and Cowtan, K. (2004). Coot: model-building tools for molecular graphics. Acta Crystallogr. D Biol. Crystallogr. *60*, 2126–2132. https://doi.org/10.1107/S0907444904019158.

33. Klaholz, B.P. (2019). Deriving and refining atomic models in crystallography and cryo-EM: the latest Phenix tools to facilitate structure analysis. Acta Crystallogr. D Struct. Biol. *75*, 878–881. https://doi.org/10.1107/S2059798319013391.

34. Schindelin, J., Arganda-Carreras, I., Frise, E., Kaynig, V., Longair, M., Pietzsch, T., Preibisch, S., Rueden, C., Saalfeld, S., Schmid, B., et al. (2012). Fiji: an open-source platform for biological-image analysis. Nat. Methods *9*, 676–682. https://doi.org/10.1038/nmeth.2019.

35. Grabner, C.P., Jansen, I., Neef, J., Weihs, T., Schmidt, R., Riedel, D., Wurm, C.A., and Moser, T. (2022). Resolving the molecular architecture of the photoreceptor active zone with 3D-MINFLUX. Sci. Adv. *8*, eabl7560. https://doi.org/10.1126/sciadv.abl7560.

36. Balzarotti, F., Eilers, Y., Gwosch, K.C., Gynnå, A.H., Westphal, V., Stefani, F.D., Elf, J., and Hell, S.W. (2017). Nanometer resolution imaging and tracking of fluorescent molecules with minimal photon fluxes. Science *355*, 606–612. https://doi.org/10.1126/science.aak9913.

37. Ostersehlt, L.M., Jans, D.C., Wittek, A., Keller-Findeisen, J., Inamdar, K., Sahl, S.J., Hell, S.W., and Jakobs, S. (2022). DNA-PAINT MINFLUX nanoscopy. Nat. Methods *19*, 1072–1075. https://doi.org/10.1038/s41592-022-01577-1.

38. Volchuk, A., Ye, A., Chi, L., Steinberg, B.E., and Goldenberg, N.M. (2020). Indirect regulation of HMGB1 release by gasdermin D. Nat. Commun. *11*, 4561. https://doi.org/10.1038/s41467-020-18443-3.

## STAR★METHODS

### KEY RESOURCES TABLE

| REAGENT or RESOURCE | SOURCE | IDENTIFIER |
| --- | --- | --- |
| **Antibodies** | | |
| anti-mouse NINJ1 (rabbit, clone 25) | Gift from Dr. Vishva Dixit and Dr. Nobuhiko Kayagaki (Genentech, Inc, South San Francisco, USA) | N/A |
| anti-human NINJ1 (sheep) | R&D | Cat. # AF5105; RRID: AB_2267337 |
| anti-human NINJ2 (rabbit) | Abcam | Cat. # ab172627 |
| anti-human ASC-Phycoerythrin (PE) | BioLegend | Cat. # 653903; RRID: AB_2564507 |
| anti-human ASC | Novus Biologicals | Cat. # NBP1-78977; RRID: AB_11015255 |
| anti-HA-tag | Cell Signaling | Cat. # 3724; RRID: AB_1549585 |
| anti-KDEL | Enzo | Cat. # ADI-SPA-827; RRID: AB_10618036 |
| anti-GM130 | BD Biosciences | Cat. # 610823; RRID: AB_398142 |
| anti-HSP60 | BD Biosciences | Cat. # 611563; RRID: AB_399009 |
| anti-sheep-HRP | Cell Signaling | Cat. # 7076S |
| anti-rabbit-HRP | Cell Signaling | Cat. # 7074S |
| Alexa Fluor® 647 AffiniPure Donkey Anti-Rabbit IgG (H+L) | Jackson ImmunoResearch | Cat. # 711-605-152; RRID: AB_2492288 |
| **Chemicals, peptides, and recombinant proteins** | | |
| Nigericin | Sigma | Cat. # N7146 |
| ABT-199 | Tocris | Cat. # 6960 |
| Lipopolysaccharide from *E. coli* serotype O55:B5 (LPS) | Sigma | Cat. # L6529 |
| Lipopolysaccharide (LPS) | Invivogen | Cat. # tlrl-b5lps |
| M-CSF | Peprotech Inc. | Cat. # 315-02 |
| MCC950 | Millipore Sigma | Cat. # 538120 |
| BODIPY™ 665/676 | Invitrogen | Cat. # B3932 |
| Phorbol 12-myristate 13-acetate (PMA) | Sigma | Cat. # P1585 |
| Doxycycline Hydrochloride | Sigma Aldrich | Cat. # D3072-1ml |
| Geneticin Selective Antibiotic (G418 sulfate) | Fisher Scientific | Cat. # 10131035 |
| Polybrene | Santa Cruz Biotechnology | Cat. # sc-134220 |
| Fugene HD | Promega | Cat. # E2311 |
| Lipofectamine 2000 | Thermo Fisher | Cat. # 11668019 |
| 4–20% Mini-PROTEAN® TGX™ Precast Protein Gels, 15-well | BioRad | Cat. # 4561096 |
| NativePAGE 3-12% gels | Thermo Fisher | Cat. # BN1001BOX |
| CellMask plasma stain | Invitrogen | Cat. # C10046 |
| 3C protease | This study | N/A |
| **Critical commercial assays** | | |
| CytoTox 96® Non-Radioactive Cytotoxicity Assay Kit | Promega | Cat. # G1780 |
| Q5 Site-Directed Mutagensis Kit | NEB | Ca. # E0552 |
| SuperSignal™ West Atto Ultimate Sensitivity Substrate kit | Sigma | Cat# A38556 |
| **Deposited data** | | |
| NINJ1 cryo-EM map deposited in the Electron Microscopy Data Resource (EMDB) under the accession number EMD-42301 | This study | EMDB: EMD-42301 |
| NINJ1 atomic coordinates deposited in the Protein Data Bank (PDB) under the accession number 8UIP | This study | PDB: 8UIP |
| **Experimental models: Cell lines** | | |
| HA-mNINJ1 iBMDM | This study | N/A |

*(Continued on next page)*

**Continued**

| REAGENT or RESOURCE | SOURCE | IDENTIFIER |
|---|---|---|
| NINJ1-GFP THP-1 | This study | N/A |
| NINJ1 KO THP-1 | This study | N/A |
| Human monocytic THP-1 | ATCC | TIB-202™ |
| Human embryonic kidney 293T cells (HEK293T) | ATCC | CRL-3216 |
| Experimental models: Organisms/strains | | |
| Mouse: C57BL/6 wildtype | The Jackson Laboratory | JAX: 000664 |
| Oligonucleotides | | |
| NINJ1 Genescript guide #6 GGCACATAGAAGGCGAAGCT | GGCACATAGAAGGCGAAGCT | addgene #125836 |
| Recombinant DNA | | |
| HA-mNINJ1 | Borges et al.[15], | N/A |
| PDB His-MBP-3C-NINJ1 | This study | N/A |
| PDB His-MBP-3C-NINJ2 | This study | N/A |
| PCDA3.1 NINJ1-TEV-GFP-FLAG | This study | N/A |
| PCDA3.1 NINJ2-TEV-GFP-FLAG | This study | N/A |
| Software and algorithms | | |
| ImageJ2 (FIJI) v2.3.0 | imagej.net/software/fij | RRID: SCR_002285 |
| Imspector v.16.3.15635-m2205-win64-MINFLUX | http://www.imspector.de | N/A |
| GraphPad Prism 9 | GraphPad | https://www.graphpad.com/scientific-software/prism/ |
| Volocity | PerkinElmer Inc | https://volocity4d.com/about |
| SBGrid consortium | Morin et al.[22] | RRID: SCR_003511 |
| CryoSPARC | Punjani et al.[23] | https://cryosparc.com/ |
| ChimeraX | Goddard et al.[24] | https://www.cgl.ucsf.edu/chimerax/ |
| Pymol | Pymol by Schrodinger[25] | https://pymol.org/2/ |
| Phenix | Adams et al.[26] | https://phenix-online.org/ |
| Other | | |
| Gold Nanoparticles 150 nm | BBI Solutions | Cat. # EM.GC150 |
| PIP2 lipid strips | Echelon Biosciences | Cat. # P-6002 |
| Amylose Resin | NEB | Cat. # E8021L |
| 5% / 0.5% LMNG/CHS Pre-Made Solution | Anatrace | Cat. # NG310-CH210 |
| 10%:1% DDM : CHS Pre-Made Solution | Anatrace | Cat. # D310-CH210 |

## RESOURCE AVAILABILITY

### Lead contact
All information and requests for further resources and reagents should be directed to and will be fulfilled by the lead contact, Hao Wu, wu@crystal.harvard.edu.

### Materials availability
All requests for resources and reagents should be directed to and will be fulfilled by the lead contact. All reagents will be made available on request after completion of a Materials Transfer Agreement.

### Data and code availability
- The cryo-EM map has been deposited in the Electron Microscopy Data Resource (EMDB) as EMDB: EMD-42301. The atomic coordinates have been deposited in the Protein Data Bank (PDB) as PDB: 8UIP.
- This paper does not report original code.
- Any additional information required to reanalyze the data reported in this paper is available from the lead contact upon request.

## EXPERIMENTAL MODEL AND SUBJECT DETAILS

### Cell lines

THP-1 (TIB-202, ATCC) cells were maintained in RPMI with GlutaMAX (Thermo Fisher Scientific, Cat. no: 11875093) supplemented with 10% FBS (Sigma), at 37 °C in 5% $CO_2$ and a humidified atmosphere. THP-1 NINJ1 KO (Clones 37, 38, 39) cells were generated using the CRISPR/cas9 genome editing procedure. THP-1 NINJ1 KO cells (Clone 39) were reconstituted with codon optimized NINJ1-GFP cloned into pLenti plasmid containing G418 selection.

### Animals and cells

Wild-type C57BL/6 animals were purchased from Jackson Laboratories (strain #000664). All animal procedures were conducted under protocols approved by the Animal Care Committee at The Hospital for Sick Children and in accordance with animal care regulation and policies of the Canadian Council on Animal Care. Mice were housed in same-sex polycarbonate cages with *ad libitum* access to food and water. Housing rooms were temperature and humidity controlled with 14:10 h light:dark cycles. Primary bone marrow derived macrophages (BMDM) were harvested from the femurs of mixed-sex cohorts of wild-type mice. Bones were then washed with PBS under sterile conditions prior to flushing the marrow by cutting the ends and centrifuging them into sterile PBS. Following a wash in phosphate buffered saline (PBS), cells were plated in DMEM with 10 ng mL$^{-1}$ M-CSF (315-02; Peprotech Inc, Cranbury, NJ). After 5 days of culture, BMDMs were detached from the dishes with TBS and 5 mM EDTA, resuspended in fresh DMEM and plated.

## METHOD DETAILS

### Constructs and cloning

Full-length human NINJ1 and NINJ2 were cloned into the pDB-His-3C-MBP vector with an HRV 3C protease linker for E. coli expression. In addition, full-length human NINJ1 was cloned into pcDNA3-TEV-GFP-FLAG LIC 6D plasmid (Addgene #166835) for mammalian expression in Expi293 cells. NINJ1 and NINJ2 mutants were made both in the pDB-His-3C-MBP and the pcDNA3-TEV-GFP-FLAG LIC 6D plasmids.

### Protein expression and purification

For E. coli expression, NINJ1 and NINJ2 constructs were transformed into BL21 (DE3) cells, grown to an OD600 of 0.6-0.8, cold shocked on ice water for 20 min, and induced overnight with 0.4 mM Isopropyl β-D-1-thiogalactopyranoside (IPTG) at 18 °C. Cells were harvested by centrifugation (4000 *g*, 20 min) and lysed by sonication in lysis buffer (25 mM Tris-HCl pH 7.5, 150 mM NaCl, 1 mM TCEP, SIGMAFAST protease inhibitor). Cell lysate was then centrifuged (40,000 *g*, 1 h); the membrane fraction was resuspended in lysis buffer supplemented with 1 % DDM: 0.1% CHS (Anatrace) and incubated for 2 h at 4 °C for extracting NINJ1 from the membrane. Following another centrifugation (40,000 *g*, 1 h), the supernatant was incubated with amylose resin for 1 h at 4 °C. Bound resin was then washed by gravity flow with 50 column volume (CV) lysis buffer with 0.1 % DDM: 0.01% CHS and eluted with 3 CV elution buffer (25 mM Tris-HCl pH 7.5, 150 mM NaCl, 1 mM TCEP, 0.1 % DDM: 0.01% CHS 50 mM maltose).

Eluted proteins from amylose resin were concentrated and cleaved overnight with 3C protease at 4 °C. These cleaved protein samples were loaded onto a step-gradient of 25%, 30%, 35%, 40% sucrose in 25 mM Tris-HCl pH 7.5, 150 mM NaCl, 1 mM TCEP, supplemented with protease inhibitor cocktail (Sigma, Cat. no: S8830) and 0.002% LMNG (x2 LMNG CMC), and ultracentrifuged for 16 h at 40,000 rpm (MLS-50 swinging-bucket rotor, Beckman). Fractions of 300 μl were collected manually from the heavy fractions of the sucrose gradient, and NINJ1-containing fractions were merged and buffer-exchanged with Zeba™ spin desalting columns (Fisher Scientific, Cat. no: PI87771) equilibrated with the buffer containing 25 mM Tris-HCl pH 7.5, 150 mM NaCl, 1 mM TCEP, supplemented with protease inhibitor cocktail (Sigma, Cat. no: S8830) and 0.002% LMNG.

For NINJ1-GFP-FLAG expression in expi293F mammalian cells, one liter cells at 3x10$^6$ cells/ml were transfected with 1 mg plasmid using polyethylenimine (3 mg/l) as transfection reagent and addition of 5 mM glycine. Cells were harvested 24 h post-transfection. They were lysed by manual homogenization in a buffer containing 25 mM Tris-HCl pH 7.5, 150 mM NaCl, 1 mM TCEP, supplemented with protease inhibitor cocktail. The lysate was centrifuged at 42,000 RPM for 1 h (45 Ti fixed-angle rotor, Beckman), and the membrane fraction was solubilized in lysis buffer supplemented with 1 % DDM: 0.1% CHS (Anatrace) was incubated for 2 h at 4 °C, followed by another centrifugation step. The supernatant was incubated with FLAG beads over night at 4 °C. NINJ1-TEV-GFP-FLAG was eluted with 100 μg/ml 3xFLAG peptide (ApexBio, Cat. no: A6001). Eluted fractions were concentrated and incubated with TEV protease at room temperature for 30 min, which was sufficient for GFP-FLAG removal. The cleaved samples were loaded onto a step-gradient of 25%, 30%, 35%, 40% sucrose in 25 mM Tris-HCl pH 7.5, 150 mM NaCl, 1 mM TCEP, supplemented with protease inhibitor cocktail (Sigma, Cat. no: S8830) and 0.002% LMNG (x2 LMNG CMC), and ultracentrifuged for 16 h at 40,000 rpm. Untagged NINJ1 was isolated from the heavy fractions of the sucrose gradient.

### *In vitro* lipid blot assay

Lipid binding assay with purified NINJ1 and NINJ2 was performed using PIP2 strip (Echelon Biosciences, Cat. no: P-6002) according to manufacturer instructions. The PIP2 strip membranes were blocked using 3% bovine serum albumin (BSA) in PNS with 0.1%

Tween 20 (PBS-T) for 1 h following by incubation for 1 h with untagged NINJ1 and NINJ2 at 2 μg/ml diluted in 3% BSA in PBS-T. Next, the membranes were washed in PBS-T for 3 times (15 min total) and the bound proteins were visualized with anti-NINJ1 (R&D AF5105) and anti-NINJ2 (Abcam ab172627) antibodies (1:10000 in PBS-T for 1 h). All steps were performed at room temperature. All samples were analyzed at the same time under the same conditions.

### In vitro liposome assay
Purified MBP-NINJ1 and MBP-NINJ2 proteins were mixed with liposomes containing 50% PC, 40% PA and 10% PI(4)P (from brain extract) at 1:3 protein: lipids ratio. The mixture was incubated for 12 h at 4 °C, together with 3C protease in order to allow MBP tag removal and NINJ1 and NINJ2 oligomerization into rings while being incorporated into liposomes. The samples were then subjected to ultracentrifugation at 40,000 rpm for 1 h for pelleting NINJ1 and NINJ2-containing fractions. The pellet fractions were visualized by negative staining EM. For cryo-EM, NINJ1 pellet fraction was further solubilized by 0.002% LMNG and subjected to sucrose gradient ultracentrifugation.

### Mutagenesis analysis in vitro and in cells
NINJ1 and NINJ2 single mutants were made using Q5 site-directed Mutagenesis kit for both pDB-His-3C-MBP and the pcDNA3-TEV-GFP-FLAG LIC 6D plasmids. E. coli expressed MBP tagged mutants were purified and tested for oligomerization via negative staining EM and sucrose gradient profiles (for NINJ1). In addition, we performed in vitro liposome assay for the mutants to test the capability of the different types of mutants to rupture liposomes in comparison to WT. For GFP tagged mutants, they were studied in HEK 293T cells by performing cytotoxicity assay and visualizing cellular localization by confocal microscopy.

### Negative-staining electron microscopy
For negative staining, 5 μl of NINJ1 and NINJ2 samples in detergents or from liposomes were placed on a copper grid (Electron Microscopy Sciences, cat. no: FCF400CU50), incubated for 1 min, washed twice with buffer containing 25 mM Tris-HCl, pH 7.5 and 150 mM NaCl, stained with 2% uranyl formate for 30 sec and air-dried. The images were collected at a Tecnai G2 Spirit BioTWIN or JEOL Transmission Electron Microscope (TEM) equipped with AMT 2k CCD camera at 49,000x magnification and 120 keV (HMS EM core facility).

### Cryo-EM data collection
A 3 μl drop containing NINJ1 in LMNG (either reconstituted from liposomes as smaller rings, or detergents as mainly large rings) at 0.5 mg/ml was applied to a Lacey Carbon grid with ultrathin carbon support (Ted Pella, Cat. no: 01824G), blotted for 4 s, plunged into liquid ethane, and flash frozen using a FEI Vitrobot Mark IV at 100% humidity and 4 °C. Grid conditions were optimized during screening and small data set collection at the Pacific Northwest Center for Cryo-EM at Oregon Health & Science University (PNCC), the University of Massachusetts Cryo-EM Core (UMASS) and the Harvard Cryo-EM Center for Structural Biology (HMS) using FEI Talos Arctica (ThermoFisher) microscopes equipped with an autoloader (200 keV, Gatan K3 direct electron detector).

Final datasets were collected at HMS using a Titan Krios microscope (ThermoFisher) operating at 300 keV and equipped with a BioQuantum Imaging Filter (Gatan) and K3 direct electron detector (Gatan). Automated data collection was performed using SerialEM software,[27] and the movies were obtained in counting mode at 105,000x magnification (0.825 Å/pix). For NINJ1 smaller rings purified from liposomes we collected 11,000 movies with 48 frames each, recorded at multiple defocus values from -1.2 to -2.4 μm and with multiple exposures per stage shift (5x4) introduced with image shift. Each movie was acquired at a dose rate 27.44 e/s per physical pixel and a total accumulated dose of 51.3 e/Å$^2$ over 1.31 s total exposure time. For NINJ1 sample with large rings purified in detergent, 15,296 movies with 47 frames each were recorded at multiple defocus values from -1 to -2.2 μm and with multiple exposures per stage shift (5x4) introduced with image shift. Each movie was acquired at a dose rate 12.588 e/s per physical pixel and a total accumulated dose of 52.08 e/Å$^2$ over 2.8 s total exposure time. Both data sets have 0.825 Å pixel size.

### Cryo-EM data processing
Cryo-EM data processing software and support was provided by SBGrid consortium.[22] Raw movies were corrected by gain reference and beam-induced motion and combined into a motion-corrected micrograph using the MotionCorr2 algorithm.[28] The defocus value for each micrograph was determined with CTFFIND4.[29] Automated particle picking was performed in CryoSPARC: helical picker[23] for large ring segments, and Topaz training and automated picking for NINJ1 small ring data set.

The dataset of NINJ1 smaller rings yielded 597,920 particles, which were extracted with no binning resulting in 0.825 Å pixel size. Several rounds of 2D classifications were applied, showing preferred top and bottom views of NINJ1 in rings of various sizes and shapes.

A dataset of NINJ1 larger rings yielded 12,907,558 ring segments. 3 rounds of 2D classification resulted in a particle stack of 626,231 segments. 1 initial model was generated with ab initio reconstruction. Helical refinement mode, followed by the non-uniform 3D refinement using C1 symmetry resulted in final cryo-EM maps at 4.3 Å resolution. The described cryo-EM workflow for this dataset is presented in Figure S2 with gold-standard Fourier shell correlation (FSC). Post-processing of the map was performed with DeepEMhancer.[30]

### Model building and structure representation

The atomic model was built using cryo-EM map obtained from the NINJ1 ring segments purified in the presence LMNG (4.3 Å resolution). Model building was performed using UCSF-Chimera[31] and Coot[32] The final model was further subjected to refinement in Phenix[26,33] with the starting model as a reference. Structure representations were generated using ChimeraX[24] and Pymol.[25]

### Generation of the HA-NINJ1 cells

iBMDM NINJ1 knock-out cell line was generated as reported.[15] This cell line was transfected with a mouse HA-NINJ1 plasmid and stable clones isolated by G418 (0.4ug/ml) resistance. Transfection was done using FuGene HD transfection reagent (Promega) according to the manufacturer's instructions. Multiple clones were isolated and validated. Cells are negative for mycoplasma.

### Generation of NINJ1 KO and NINJ1-GFP cell lines

To generate NINJ1 KO and single-guide RNA (sgRNA) control THP-1 cells, we transduced THP-1s (early passage, ATCC) with lenti-CRISPR v2 (NINJ1 Genescript guide #6 GGCACATAGAAGGCGAAGCT, addgene #125836). For lentivirus preparation, $0.5 \times 10^6$ HEK293T cells in 6-well dishes were transfected (6 μL Fugene) with 1 μg of plasmid containing the construct of interest, 750 ng psPAX2 packaging plasmid and 250 ng pMD2.G envelope plasmid (Addgene plasmids #12260 and #12259). On the following day the medium was changed, and the virus-containing medium was collected an additional 24 h later. Virus-containing medium was concentrated with LentiX concentrator (Takara) and resuspended in RPMI (20X concentration). 1 million THP-1 cells seeded in 6-well plates were spinfected with 100 μL concentrated virus in 900 μL medium (2 h, 30 degrees, 1000 x g) containing 8 ug/mL polybrene. Following spinfection, THP-1 cells were recovered in fresh medium for 2 d prior to puromycin selection (3 μg/mL) for 3 days. Selected cells were single cell sorted into 96 well format with a BD FACSAria II cell sorter equipped with 100 μm nozzle. Cells were expanded before screening clones by western blot and subsequent genomic sequencing. We obtained 3 clones (37,38,39) in which NINJ1 was undetectable by western blot. Among the 3 clones, we used clone 39 for subsequent experiments given it had biallelic frameshift mutations (1 and 11 bp). For reconstituting NINJ1 KO cells with Doxycycline-inducible NINJ1-GFP (pInducer20), we produced virus and spinfected NINJ1$^{-/-}$ THP-1 cells as above. Cells were selected with 250 μg/ml G418 for 2 weeks prior to use in further experiments.

### Pyroptosis and secondary necrosis induction

In primary BMDMs and THP-1 cells pyroptosis was activated in cells primed with (0.5 μg/ml) LPS from *E. coli* serotype 055:B5 (Invivogen, Cat. no: tlrl-b5lps), which was first reconstituted at a stock concentration of 1 mg/ml. Cells were primed with LPS for a total of 4 hours, followed by induction with 10 μM or 20 μM nigericin (Sigma N7143; stock 10 mM in ethanol) for the final 15 min, 30 min or 60 min. Secondary necrosis was induced using ABT-199 in primary BMDMs (Tocris, 6960).

### Immunoblotting of whole cell lysates

NINJ1-GFP cells were seeded at $0.7 \times 10^6$ cells/well on a 6-well tissue culture plate and treated with 25 ng/ml phorbol 12-myristate 13-acetate (PMA, P1585, Sigma) for 2 days and then recovered with complete medium (without PMA) for 24 h and supplemented with 1 μg/ml Doxycycline (Dox) or no Dox as a control. On the next day, cells were untreated or primed with 1 μg/ml LPS (Invivogen, Cat. no: tlrl-b5lps) for 4 h, followed by 1 h incubation with 10 μM nigericin (Sigma-Aldrich, Cat. no: N7143-5MG) for cell death stimulation. While collecting cells, we collected both pellet and supernatant fractions. The pellet fractions were collected by scraping cells with cell lifter with PBS and spinning at x 500 g for 5 min. The supernatant fractions were first spun down at 500 g for 5 min and then concentrated using 10K cutoff Centricon. SDS sample buffer was added to equal number of cells (by volume) and loaded to 4-20% non-reducing gel for western blot analysis. Moreover, in an additional analysis the concentrated supernatant fraction was ultracentrifuged for 1 hr at 136,000x g following western blot analysis for the pellet fraction Western blotting was performed using anti-NINJ1 (1:1000, R&D AF5105) and anti-sheep-HRP (1:5000, Cell Signaling, Cat. no: 7076S) secondary antibody.

### Blue-native PAGE of NINJ1

Primary mouse BMDMs were plated onto 10 cm dishes and treated as indicated in the figure legend. Following treatments, the supernatant (medium) was collected from each dish for centrifugation at 500 x *g* for 5 minutes, followed by 3000 x *g* for 10 min. Next, supernatant samples were concentrated using Centricon Plus-70 centrifugal filters (Millipore, UFC701008), after which the protein concentration of samples was determined using the BioRad DC protein concentration assay kit (5000112) as per the manufacturer's instructions. 4 μg of sample was mixed with 4x NativePAGE sample buffer and Coomassie G-250 (ThermoFisher) and resolved using NativePAGE 3-12% Bis-Tris gels, transferred onto polyvinylidene difluoride (PDVF) membranes, and immunoblotted using rabbit monoclonal anti-mouse NINJ1 primary antibody (clone 25; kind gift from Dr. Kayagaki and Dr. Dixit at Genentech, Inc.).[3]

### Immunofluorescence (IF)

NINJ1-GFP THP-1 cells were plated on CELLview 4-compartment dishes (Greiner Bio-One), treated with 25 ng/ml phorbol 12-myristate 13-acetate (PMA, P1585, Sigma) for 2 days, and then incubated for 24 h with complete medium without PMA and supplemented with 1 μg/ml Doxycycline (Dox) or without Dox as a control. Cells were untreated or primed with 1 μg/ml LPS (Invivogen, Cat. no: tlrl-b5lps) for 4 h, followed by 1 h incubation with 10 μM nigericin (Sigma-Aldrich, Cat. no: N7143-5MG). Cells were fixed

in 3% paraformaldehyde (PFA) for 30 min at 4 °C and permeabilized with 0.1% Triton X-100 for 10 min. Cells were incubated in PBS-Tween containing 3% BSA for 3 h, which minimized non-specific binding. After three washes with PBS-Tween, cells were incubated overnight at 4 °C with primary antibodies (human ASC 1:1000, Novus Biologicals, NBP1-78977 and human ASC-Phycoerythrin (PE) 1:1000, BioLegend 653903). NINJ1 was detected by the GFP signal, and no antibody was required in order to enhance the signal. After incubation, cells were washed and incubated with AlexaFluor647-conjugated anti-rabbit IgG (1:750, ThermoFisher, Cat. no: A27040) for 1 h at room temperature, washed with PBS (3 x 10 min) and then stained with Hoechst (1:500, Immunochemistry Technologies, Cat. no: 639). Cells were imaged using a Nikon Ti inverted microscope fitted with a Photometrics CoolSNAP HQ2 Peltier cooled CCD camera and Andor Zyla 4.2 sCMOS camera at x60 magnification using Plan Apo 60x/1.3 DIC objectives. Lumencor SpectraX LED illuminator was used. Chroma 49000 (DAPI), Chroma 29002 (green) and Chroma 49011 (far red) filter cubes were used. Image analysis was performed in Fiji[34]

### Live cell imaging
NINJ1-GFP THP-1 cells were cultured in RPMI supplemented with GlutaMAX (Thermo Fisher Scientific, Cat. no: 11875093) supplemented with 10% FBS (Sigma) and neomycin (G418), at 37°C in 5% CO2 atmosphere. Cells treatment was carried out as for IF (above). For performing live cell imaging, we imaged LPS primed cells, induced with Dox for 24 h. Cells were imaged using a Nikon Ti inverted microscope fitted with a Photometrics CoolSNAP HQ2 Peltier cooled CCD camera and Andor Zyla 4.2 sCMOS camera at x60 magnification using Plan Apo 60x/1.3 DIC objective. Green and bright field channels were used. Time lapsed imaging was started upon addition of 10 μM nigericin. Images were recorded for over an hour with 2 min intervals. Image analysis was performed in Fiji[34]

### Lipid labeling of whole cell lysates
Concentrated NINJ1-GFP THP-1 activated cells were labeled with BODIPY™ 665/676 (Invitrogen B3932) at a final dye concentration of 10 μg/ml followed by 10%-40% sucrose ultracentrifugation. The pellet fraction was analyzed by spinning disk confocal imaging and negative staining EM. Confocal image analysis and plot profiles were performed in Fiji[34]

### LDH assay
HEK 293T cells were seeded at 100,000 per well in 96-well plates, and NINJ1 constructs were transfected with lipofectamine 2000 with 0.25 μg DNA per well. 24 h following transfection, cell supernatants were analyzed for LDH activity using the CytoTox 96® Non-Radioactive Cytotoxicity Assay Kit (Promega, Cat. No: G1780). The samples' absorbance at 490 nm was measured by a bioTEK plate reader.

### Minimal photon fluxes (MINFLUX) nanoscopy
Primary cells from wild-type animals were harvested as described above and cultured on 1.5H glass coverslips. Cells were primed with LPS and stimulated to undergo pyroptosis as described above. Pyroptosis induction was confirmed by LDH release for each experimental replicate. Following treatments, cells were washed with PBS and fixed in 4% paraformaldehyde and 0.1% glutaraldehyde in 0.1 M cacodylate buffer at room temperature for 15 min. The cells were washed 3 times in PBS, permeabilized with 0.1% Tween-20, then blocked in 10% donkey serum and 0.1% Tween-20 in PBS for 1 h in PBS. Rabbit monoclonal anti-mouse NINJ1 primary antibody (clone 25[3] at 10 μg/mL was then added overnight at 4 °C. The cells were washed three times with PBS supplemented with 0.1% Tween-20 before the addition of secondary antibody in PBS with 1% donkey serum for 1 h at room temperature. Alexa Fluor-647-conjugated donkey anti-rabbit secondary antibody (711-605-152) was used at a 1:1000 dilution. The samples were then washed with PBS and stabilized for MINFLUX imaging using 150 mm gold nanoparticles (EM.GC150, BBI Solutions) for 5-10 min, then mounted in imaging buffer, 50 mM Tris-HCl, 10 mM NaCl, 10% (w/v) glucose, and 64 μg/mL catalase, 0.4 mg/mL glucose oxidase, and 10 to 25 mM mercaptoethylamine, pH 8.0, as previously described,[35,36]

A MINFLUX microscope (Abberior Instruments) equipped with a spatial light modulator-based beam shaping module and an electro-optical detector-based MINFLUX was used. Microscopy and MINFLUX measurements were performed using Imspector Software (v.16.3.15635-m2205-win64-MINFLUX; RRID:SCR_015249) using MINFLUX sequence templates seqIIF and DefaultIIF3D for 2D- and 3D-MINFLUX measurements as previously described.[37] Molecular precision was enabled through a reflection-based stabilization unit based on a 980-nm as previously described.[16] Before starting each MINFLUX measurement, the stabilization of the microscope was activated. Measurements were conducted with a stabilization precision of < 1 nm. A 642 nm (CW) excitation laser, a 405 nm activation laser, and detection windows in the range of 650-750 nm were used. The emitted fluorescence photons were counted using two avalanche photodiodes with the appropriate fluorescence filters. Molecular precision was enabled through a reflection-based stabilization unit based on a 980-nm laser as previously described.[16] For structure counting and ring-like structure diameter measurements, localizations were exported as 2D projections with a pixel size of 4 nm (2D) or 5-6 nm (3D) using Imspector Software. Individual structures were counted in ImageJ and classified according to shape: ring-like, punctate, or other. The diameter of each ring-like structure was considered as the largest measurable distance between points with zero localizations in the structure center and measured using the line tool in ImageJ-Fiji Software.

### Mouse NINJ1 co-localization and imaging

For immunofluorescence labelling, iBMDMs stably expressing HA-NINJ1 cells were seeded onto glass coverslips. The next day the cells were treated or not with LPS (0.5 μg/mL) for a total of 3.5 h, during which nigericin (10μM) was added for the final 1 h. Cells were then washed with PBS and permeabilized using 0.1% Triton X-100 in PBS for 5 min and blocked with 1% BSA in PBS for 1 h. Cells were incubated with primary antibodies for 1 h, washed, then incubated with Alexa Fluor-488 or Cy3-conjugated secondary antibodies for 1 h. Prior to imaging, cells were stained with DAPI for 5 min. Antibodies used: anti-HA-tag (Cell Signaling, 3724), anti-KDEL (Enzo, ADI-SPA-827), anti-GM130 (BD Biosciences, 610823), anti-HSP60 (BD Biosciences, 611563).

Cells were imaged as described in[38] by spinning disk confocal microscopy (Quorum) on a Zeiss Axiovert 200M microscope with a ×63 objective and an additional ×1.5 magnifying lens. Images were acquired by a CCD camera (Hamamatsu Photonics) driven by Volocity software.

## QUANTIFICATION AND STATISTICAL ANALYSIS

Statistical testing was calculated using Prism 9.0 (GraphPad Software Inc, La Jolla, CA; RRID:SCR_002798). Groups were compared using Student t test for two groups. Unless specified otherwise, all collected data was analyzed and a P value < 0.05 was considered statistically significant.

# Supplemental figures
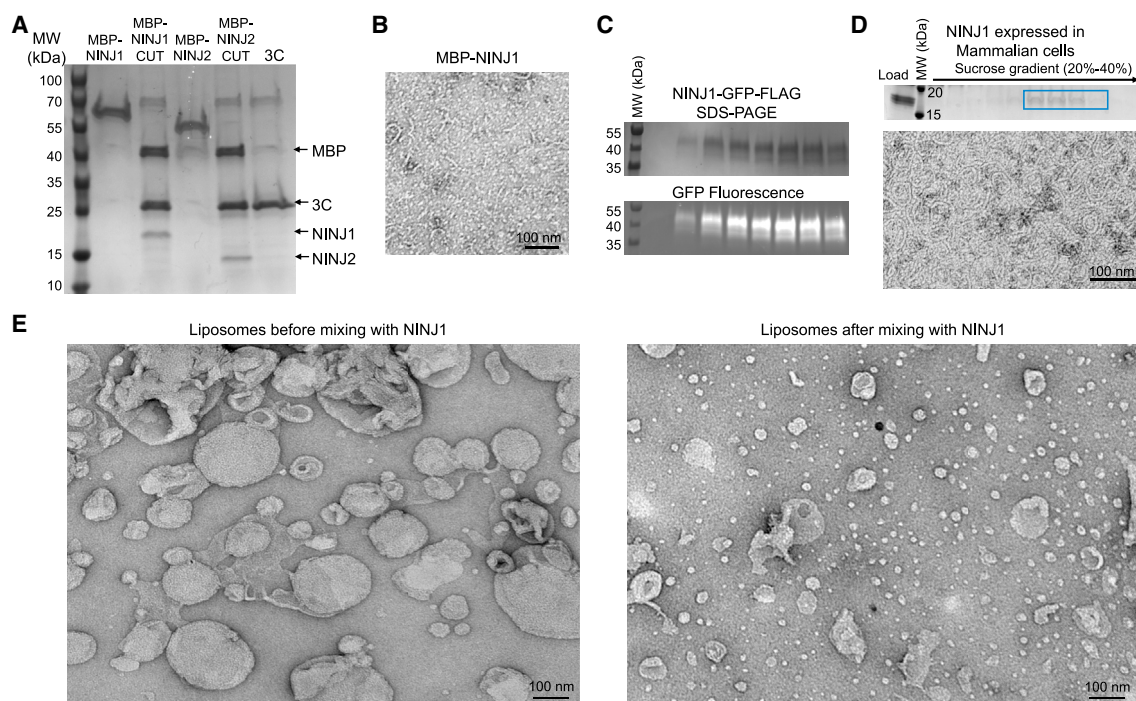


**Figure S1. NINJ1 and NINJ2 purification, related to Figure 1**

(A) SDS-PAGE of MBP-NINJ1 and MBP-NINJ2 purification from *E. coli* expressed.

(B) Negative staining EM image of MBP-NINJ1. NINJ1 large rings were hardly detected before MBP removal.

(C) SDS-PAGE of NINJ1-GFP-FLAG purification and detection by in-gel GFP fluorescence at the expected molecular weight.

(D) SDS-PAGE (top) and negative staining EM image (bottom) of NINJ1-GFP-FLAG after GFP-FLAG removal by TEV.

(E) Liposome breakdown by NINJ1, shown by negative staining EM images before and after NINJ1 incorporation into liposomes. Liposome membrane breakdown by NINJ1 is clearly shown.

All data are representative of three or more independent experiments.
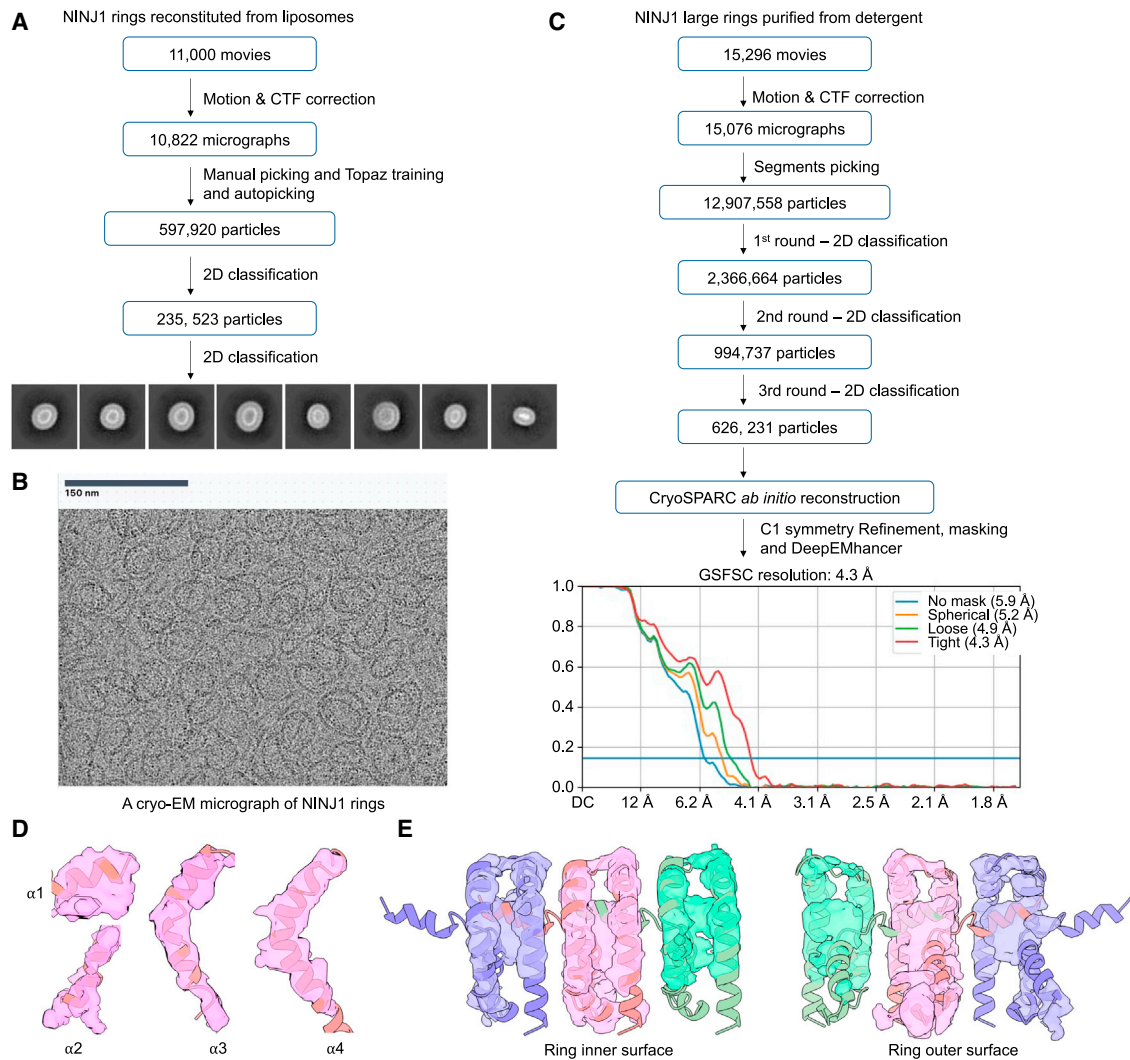
**Figure S2. Cryo-EM flow charts of NINJ1 data processing, related to Figure 2**

(A) Flow chart for cryo-EM data processing of NINJ1 rings reconstituted from liposomes.

(B) A raw cryo-EM micrograph of NINJ1 large rings in detergent.

(C) Chart flow for cryo-EM data processing of NINJ1 large ring segments purified from detergent.

(D and E) NINJ1 subunits fitted in the cryo-EM map viewed for individual helices (D); the hydrophobic, concave side of the ring (E, left); and the hydrophilic, convex side of the ring (E, right).

**A**



High density region from the TM helices α3 and α4 and possibly α1 – facing the inside of the ring

Low density region from mainly α2 – facing the outside of the ring

**B**



**C**



THP1 cells

Control*    NINJ1 KO

WT  1  2  3   37  38  39

Cas9

NINJ1

GAPDH

*Control KO with Cas9 and control sgRNA

**D**

```
GenScript gRNA 6: GGCACATAGAAGGCGAAGCT

CTG ATG GCC AAC GCG TCC CAG CTG AAG GCC GTC GTG GAA CAG GGC CCC AGC TTC GCC TTC TAT GTG CCC CTG GTG
 L   M   A   N   A   S   Q   L   K   A   V   V   E   Q   G   P   S   F   A   F   Y   V   P   L   V
57                                                                                               81

Clone 37:
CTG ATG GCC AAC GCG TCC CAG CTG AAG GCC GTC GTG GAA CAG GGC CCC AGC TTC GCC TTC TAT GTG CCC CTG GTG

(24 bp deletion/22 bp deletion)
CTG ATG GCC AAC GCG TCC CAG CTG AAG GCC GTC GTG GAA CAG GGC CCC AG- --- --- --- --- --- --- --- GTG
CTG ATG GCC AAC GCG TCC CAG CTG AAG GCC G-- --- --- --- --- --- --- --- -CC TTC TAT GTG CCC CTG GTG

Clone 38:
CTG ATG GCC AAC GCG TCC CAG CTG AAG GCC GTC GTG GAA CAG GGC CCC AGC TTC GCC TTC TAT GTG CCC CTG GTG

(21 bp deletion/51 bp deletion)
GCG AT- --- --- --- --- --- --- --G GCC GTC GTG GAA CAG GGC CCC AGC TTC GCC TTC TAT GTG CCC CTG GTG
CTG ATG GCC AAC GCG --- --- --- --- --- --- --- --- --- --- --- --- --- --- --- --- --- CCC CTG GTG

Clone 39:
CTG ATG GCC AAC GCG TCC CAG CTG AAG GCC GTC GTG GAA CAG GGC CCC AGC TTC GCC TTC TAT GTG CCC CTG GTG

(1 bp deletion/11 bp deletion)
CTG ATG GCC AAC GCG TCC CAG CTG AAG GCC GTC GTG GAA CAG GGC CCC AGC -TC GCC TTC TAT GTG CCC CTG GTG
CTG ATG GCC AAC GCG TCC CAG CTG AAG GCC GTC GTG GAA CAG G-- --- --- --- GCC TTC TAT GTG CCC CTG GTG
```

**Figure S3. Structural representation on NINJ1 ring segments, related to Figures 2 and 3**

(A) Model of a longer NINJ1 ring segment, showing the high-density face labeled in deep purple and the low-density face labeled in orange, based on the 2D classification shown in (B).

(B) 2D classification of NINJ1 ring segments, showing that all classes possess a high-density concave face and a low-density convex face.

(C) Western blots of anti-Cas9, anti-NINJ1, and anti-GAPDH (loading control) for WT, control sgRNA cells, and single NINJ1 knockout clones. The data are representative of three or more independent experiments.

(D) Genomic sequencing for NINJ1 KO clones (clones 37, 38, and 39).

**A** NINJ1 KO THP-1 with Dox-inducible NINJ1-GFP NINJ1



**B** NINJ1 KO THP-1 with Dox-inducible NINJ1-GFP NINJ1



**C** NINJ1 KO iBMDM with HA-NINJ1



**D**



**E**



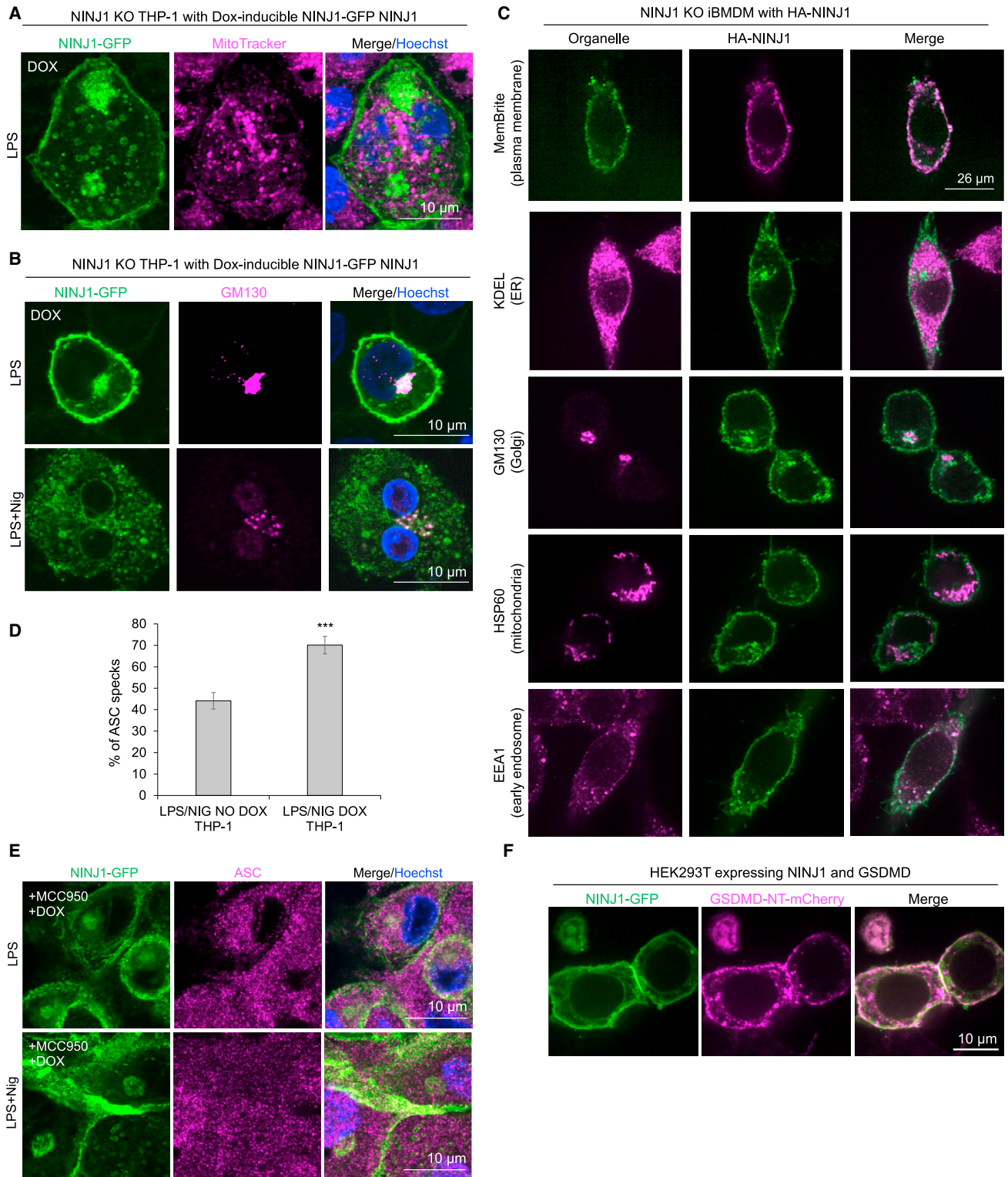**F** HEK293T expressing NINJ1 and GSDMD



**Figure S4. Immunofluorescence imaging of NINJ1 and organelle localization, related to Figure 3**

(A) Confocal imaging of LPS-primed Dox-induced NINJ1-GFP cells (green), stained with the mitochondria marker MitoTracker (magenta), and DNA (Hoechst dye, blue). Scale bars, 10 μM.

*(legend continued on next page)*

(B) Immunofluorescence (IF) confocal imaging of LPS-primed or LPS/nigericin-treated Dox-induced NINJ1-GFP cells (green) for the Golgi marker GM130 (magenta) and DNA (Hoechst dye, blue). Scale bars, 10 μM.

(C) IF confocal imaging of NINJ1 KO iBMDMs reconstituted with HA-NINJ1 (green or magenta) cells co-localized with the following organelle markers: MemBrite (green, for plasma membrane), KDEL (magenta, for endoplasmic reticulum [ER]), GM130 (magenta, for Golgi), HSP60 (magenta, for mitochondria), and EEA1 (magenta, for early endosome). Scale bars, 26 μM.

(D) Quantitative analysis of IF experiments of ASC speck formation upon LPS/nigericin activation of NINJ1 KO THP-1 cells reconstituted with Dox-inducible NINJ1-GFP, fixed and imaged 24 h after Dox introduction, or DMSO as a control. Data shown are mean ± SEM based on n = 3 fields of view for each condition. Statistical significance was assessed by 2-tailed t test. *** denotes $p < 0.0001$.

(E) IF confocal imaging of Dox-induced NINJ1-GFP THP-1 cells in the presence of NLRP3 inhibitor MCC950, in the presence of LPS or LPS + nigericin, visualized for NINJ1 (green), ASC (magenta), and DNA (Hoechst dye, blue). Scale bars, 10 μM.

(F) Confocal imaging of transiently co-expressed NINJ1-GFP and GSDMD-NT-mCherry, imaged 24 h after DNA transfection and visualized by NINJ1 (green), GSDMD (magenta), and DNA (Hoechst dye, blue). Scale bars, 10 μM.

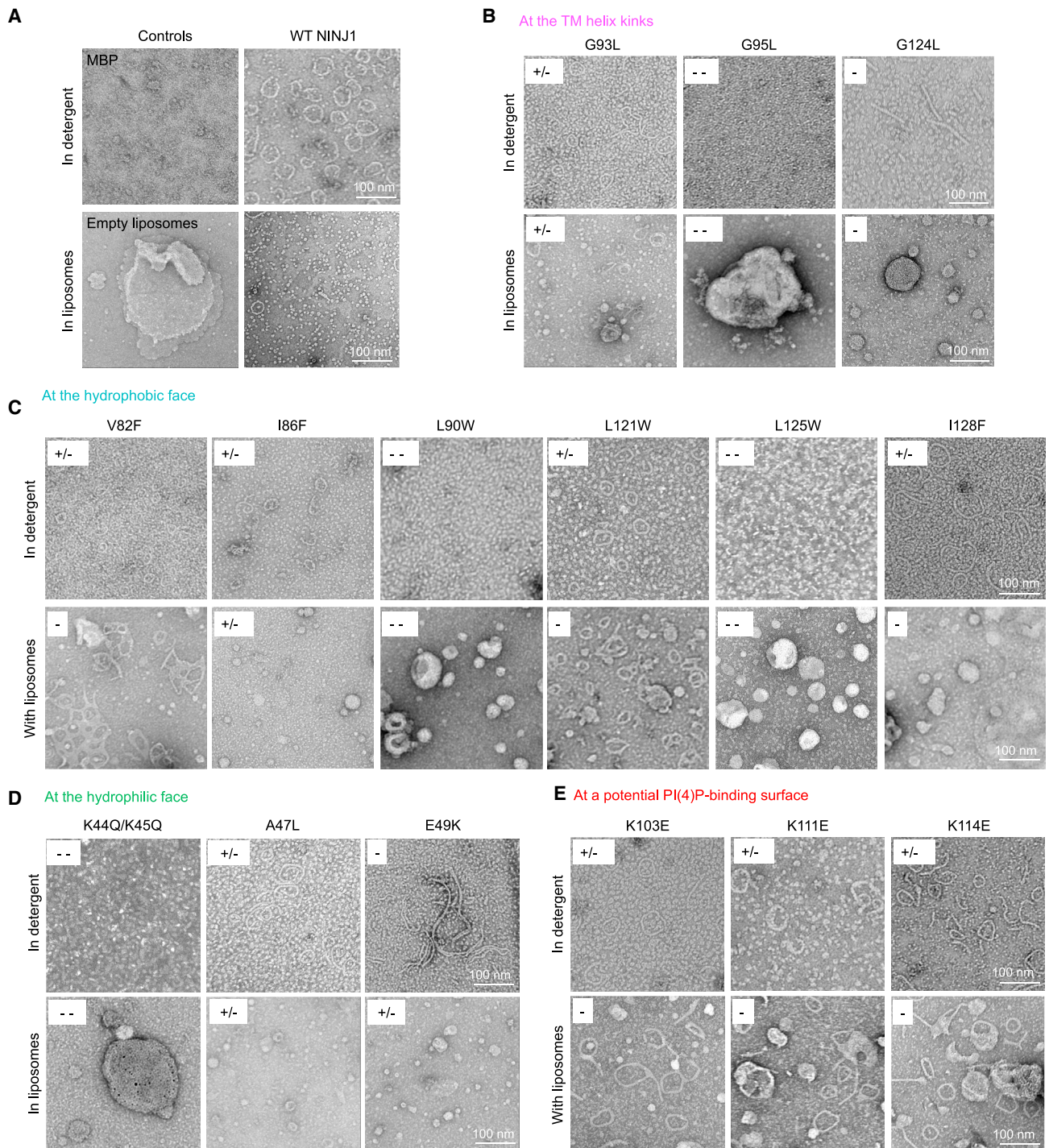Data in (A) and (B) and (E) and (F) are representative of three or more independent experiments.

**Figure S5. EM imaging of purified NINJ1 mutants in detergents and in reconstituted liposomes, related to Figure 5**

(A–E) Negative staining EM images to examine NINJ1-containing structures in detergents and with liposomes for WT NINJ1 and MBP control (A), mutants at the TM helix kinks (B), mutants at the hydrophobic face (C), mutants at the hydrophilic face (D), and mutants at a potential PI(4)P-binding surface. The scores for oligomerization and liposome rupture relative to WT NINJ1 are shown at the top left corner of each image. For oligomerization, + = many rings as for WT NINJ1; +/− = some filaments and rings in a background of small dots; − = a few filaments in a background of small dots; − − = barely any rings or filaments with only a background of small dots. For liposome rupture, + = dissolved small rings as for WT NINJ1; +/− = small rings plus a few undissolved liposomes; − = lots of undissolved liposomes; − − = largely undissolved liposomes.

All data are representative of three or more independent experiments.
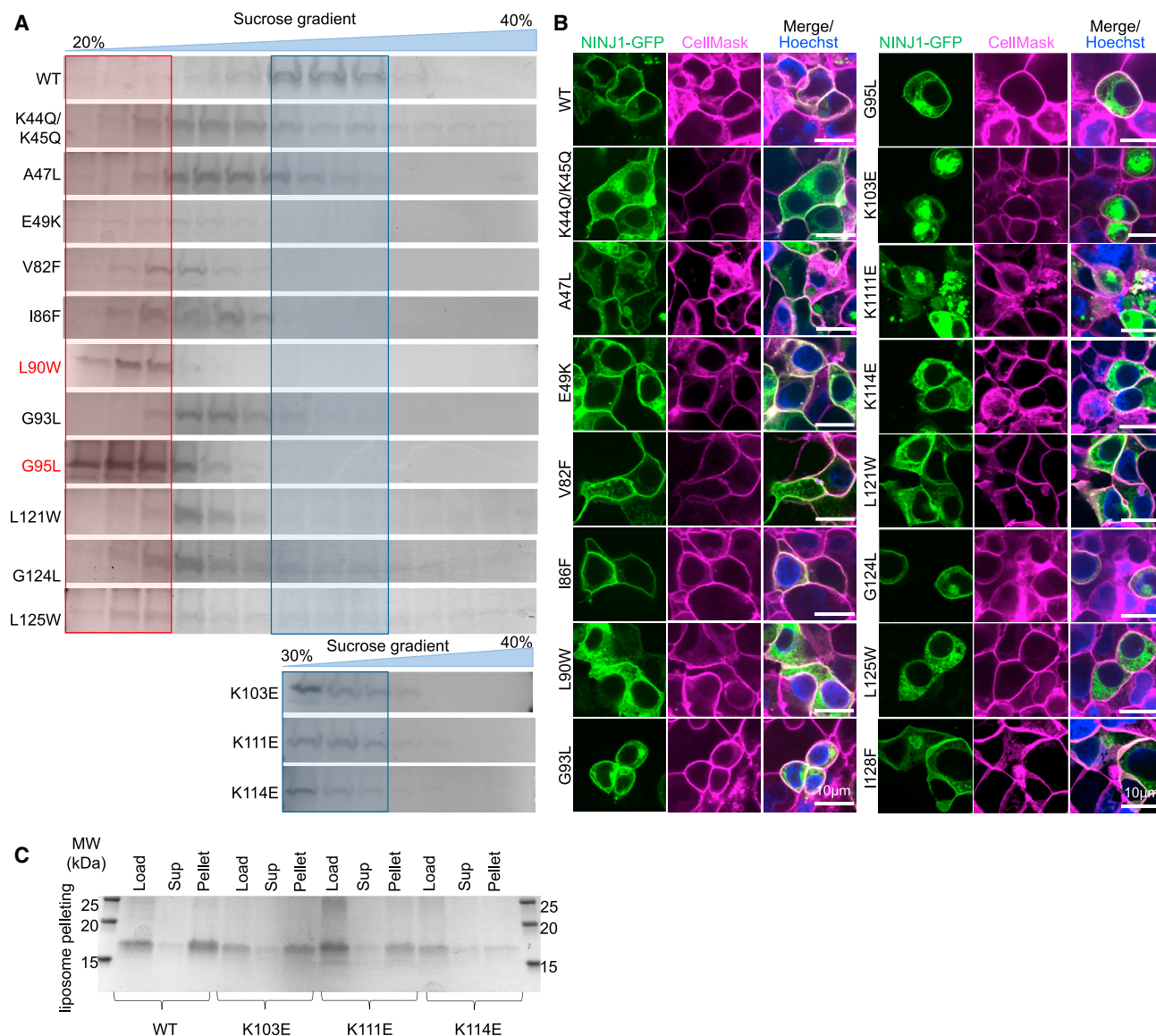
**Figure S6. Oligomerization of NINJ1 mutants by sucrose gradient and cellular localization in HEK 293T cells, related to Figure 5**

(A) Sucrose gradient profiles of purified NINJ1 mutants in comparison to NINJ1 WT.

(B) Confocal imaging of GFP-tagged NINJ1 WT and mutants (green) co-stained with the plasma membrane dye, CellMask (magenta), and DNA (Hoechst dye, blue). Cells were fixed 24 h after DNA transfection and imaged.

(C) SDS-PAGE of liposome pelleting assay for NINJ1 mutants at the potential PI(4)P-binding surface. Sup, supernatant.

All data are representative of three or more independent experiments.

**A**

| NINJ2 | WT | V86F | Q103K | I110G | F114I |
|---|---|---|---|---|---|
| Oligomerization into rings/filaments | + | + | +/- | - | +/- |
| Liposome rupture | - - | - - | - | - | - |
| Cell death (LDH release) | - - | - | - | - | - |
| Plasma membrane localization | + | + | + | + | + |
| New in this paper | | New | * | New | * |

*Also tested in Degen et al. (Degen *et al.*, 2023)

**B**



**C**



**D**



**E**



**F**



**G**



**H**



Figure S7. Analysis of NINJ2 mutants and NINJ1 MINFLUX microscopy during secondary necrosis, related to Figures 5 and 6

(A) A table summarizing the mutational analysis *in vitro* and in cells for NINJ2 mutants. The mutants were scored based on the following assays: (i) oligomerization by EM imaging, (ii) liposome rupture, (iii) cell death (LDH release), and (iv) plasma membrane localization by confocal imaging.

(B) Negative staining EM imaging of purified NINJ2 mutants in detergents and in reconstituted liposomes.

(C) Confocal imaging of GFP-tagged NINJ2 WT and mutants (green) co-stained with the plasma membrane dye, CellMask (magenta), and DNA (Hoechst dye, blue). Cells were fixed 24 h after DNA transfection and imaged. Scale bars, 10 μM.

(D) Cytotoxicity assay of NINJ2 and mutants in HEK293T cells measured based on % of LDH release at 24 h post transfection. Data shown are as mean ± SEM of three or more independent experiments. Statistical significance was assessed by a 2-tailed t test. ** and * denote $p < 0.001$ and 0.01, respectively.

(E) Blue-native PAGE gel and western blot of endogenous NINJ1 in the supernatant of primary BMDMs upon pyroptosis activation in comparison to LPS-treated cells.

(F) 2D-MINFLUX images (confocal inset) of primary mouse BMDMs without (control, left) or with secondary necrosis stimulation (ABT-199, right). The BMDMs were stimulated by treatment with ABT-199 or DMSO (vehicle). Cells were fixed in 4% paraformaldehyde and 0.1% glutaraldehyde, followed by immunolabelling with anti-NINJ1 antibody (rabbit monoclonal clone 25, Genentech, Inc) and Alexa Fluor 647-conjugated whole IgG secondary antibody. Top: samples were imaged by MINFLUX. Small dashed white boxes indicate images shown in (bottom). Scale bars, 500 nm. Bottom: representative structures of each classification category for ABT-199-treated cells, ring-like (i), discrete puncta (ii), or other (iii). Scale bars, 40 nm.

(G) Pie charts for NINJ1 structures counted and classified as ring-like, discrete puncta, or other for control BMDMs (DMSO) and those stimulated to undergo secondary necrosis (ABT-199).

(H) A graph of the largest measured inner diameters of the identified ring-like structures in the 2D plane, shown with a median of 23.9 nm (interquartile range, 21.0–65.8 nm).

Data in (B) and (C) are representative of three independent experiments, and data in (F)–(H) are representative of two independent experiments.